

Inertial waves in a differentially rotating spherical shell

C. BARUTEAU¹† AND M. RIEUTORD²

¹Department of Applied Mathematics and Theoretical Physics, University of Cambridge, Wilberforce Road, Cambridge CB3 0WA, United Kingdom

²Institut de Recherche en Astrophysique et Planétologie, CNRS et Université de Toulouse, 14 avenue E. Belin, 31400 Toulouse, France

(Received 19 March 2012; revised 19 October 2012; accepted 30 November 2012)

We investigate the properties of small-amplitude inertial waves propagating in a differentially rotating incompressible fluid contained in a spherical shell. For cylindrical and shellular rotation profiles and in the inviscid limit, inertial waves obey a second-order partial differential equation of mixed type. Two kinds of inertial modes therefore exist, depending on whether the hyperbolic domain where characteristics propagate covers the whole shell or not. The occurrence of these two kinds of inertial modes is examined, and we show that the range of frequencies at which inertial waves may propagate is broader than with solid-body rotation. Using high-resolution calculations based on a spectral method, we show that, as with solid-body rotation, singular modes with thin shear layers following short-period attractors still exist with differential rotation. They exist even in the case of a full sphere. In the limit of vanishing viscosities, the width of the shear layers seems to weakly depend on the global background shear, showing a scaling in $E^{1/3}$ with the Ekman number E , as in the solid-body rotation case. There also exist modes with thin detached layers of width scaling with $E^{1/2}$ as Ekman boundary layers. The behavior of inertial waves with a corotation resonance within the shell is also considered. For cylindrical rotation, waves get dramatically absorbed at corotation. In contrast, for shellular rotation, waves may cross a critical layer without visible absorption, and such modes can be unstable for small enough Ekman numbers.

Key words: rotating flows — waves in rotating fluids

1. Introduction

The fluid flows that pervade the interior of stars and planets are most of the time dominated by a strong background rotation. The Earth's atmosphere, oceans, or its liquid core are typical examples. Such flows are studied in a rotating frame, and the dominance of rotation arises through that of the Coriolis acceleration over all other terms in the momentum equation (the centrifugal acceleration is usually combined with the pressure gradient through the so-called reduced pressure). The Coriolis acceleration implies that the response of a rotating fluid to small amplitude oscillations may become singular.

It is known indeed since the work of Cartan (1922) that the pressure perturbations of an inviscid incompressible fluid obey Poincaré equation, which has the remarkable property of being spatially hyperbolic. Since boundary conditions have to be met by solutions, oscillations of bounded rotating fluids are a mathematically ill-posed problem. It means that, in most general containers, eigenmodes of inviscid incompressible fluids may simply not exist. Mathematically, the point spectrum of the operator is said to be empty. However, a few containers such as the full ellipsoid or the cylindrical layer allow the existence of such eigenmodes, because of the separation of spatial variables that is possible in these geometries. Solutions were worked out by Kelvin (1880) for the cylinder, and by Bryan

† Email address for correspondence: C.Baruteau@damtp.cam.ac.uk

(1889) for the sphere and the ellipsoid. The singular nature of the solutions to Poincaré equation have been uncovered almost a century later by the works of Stewartson & Rickard (1969) and Stewartson (1971, 1972a). Stewartson (1972b) showed that these singularities should turn into oscillating shear layers through viscosity.

New interest into the singular solutions to the Poincaré equation was put forward with the work of Maas & Lam (1995) on gravity modes in two-dimensional basins. The pressure fluctuations of internal gravity modes also satisfy Poincaré equation, and Maas & Lam (1995) showed the crucial role of characteristic trajectories and coined the concept of attractor to describe the convergence of characteristics to special limit cycles. At the same time, Hollerbach & Kerswell (1995) and Kerswell (1995) investigated the internal shear layers spawned by the critical latitude singularity (another singularity different from that of the attractors), in relation with the precession flows of a spherical shell.

Subsequent work by Rieutord & Valdettaro (1997), Rieutord *et al.* (2001) and Rieutord *et al.* (2002) demonstrated how attractors feature the oscillations of slightly viscous rotating fluids contained in spherical shells. For very small viscosities, relevant to astrophysical and geophysical applications, oscillating flows are confined within shear layers that closely follow attractors of characteristics. In the two-dimensional limit of a spherical shell, Rieutord *et al.* (2002) derived analytical solutions for the structure of shear layers. They showed in particular that the velocity field of eigenmodes obeys the same equation as that governing the quantum states of a particle trapped in a parabolic well (the Schrödinger equation).

More recently, forced oscillations in rotating fluids have been examined in the context of tidal interactions between two celestial bodies (Ogilvie & Lin 2004; Wu 2005; Ogilvie & Lin 2007; Goodman & Lackner 2009; Ogilvie 2009; Rieutord & Valdettaro 2010). Dissipation of tidally-forced modes of oscillations in each companion alters the orbital elements and spin of each body. It plays a prominent role in the late evolution of close-in extrasolar planets. The efficiency of tidal dissipation mechanisms is usually parametrized by a single, dimensionless tidal quality factor Q , which is an inverse measure of the tidal torque acting on a gravitationally perturbed body. However, tidal dissipation is extremely sensitive to the frequency and amplitude of the external tidal potential (see, e.g., Ogilvie 2009; Rieutord & Valdettaro 2010). This dependency is intimately related to the existence of singularities arising from the hyperbolic nature of the Poincaré equation. As in free modes of oscillations, these singularities consist of the critical latitude singularity and attractors of characteristics.

Works examining tidal dissipation mechanisms in rotating fluids have used simple fluid models, where the background flow disturbed by inertial modes is in pure solid-body rotation. The rotation pattern inside stars and planets is much more intricate, as may be guessed. Large-scale flows are usually present in stars and planets. Most frequently, such flows are largely axisymmetric, and include differential rotation as well as a weak meridional circulation. In light of previous works on rigidly rotating fluids, the present paper is a first study of how departure to solid-body rotation impacts the oscillation properties of rotating fluids and their associated tidal dissipation. In this first paper, we focus on free inertial modes of oscillations. Tidally-forced inertial modes will be examined in a future study. As a first simplification, we discard meridional circulation, which is very weak in general, especially for very small viscosities. However, the choice for the differential rotation pattern, which we assume to be axisymmetric, remains open. The azimuthal velocity of the (smooth) differentially rotating background flow can be expanded into spherical harmonics,

$$u_\varphi(r, \theta) = - \sum_{\ell} w_m^\ell(r) \partial_\theta Y_\ell^m ,$$

as for any axisymmetric azimuthal component of a vector field (Rieutord 1987). In this expression, r , θ , and φ denote the usual spherical coordinates, Y_ℓ^m the spherical harmonics normalized on the sphere of unit radius, and $w_m^\ell(r)$ accounts for the radial variation in the

flow. If differential rotation is smooth, we expect the previous expansion to be dominated by small ℓ 's. In the present work, we will primarily focus on a single term, the $\ell=1$ -term, such that the background velocity field takes the form

$$u_\varphi(r, \theta) = w(r) \sin \theta = r\Omega(r) \sin \theta,$$

with differential rotation along the radial direction only (Ω denotes the local angular frequency of the fluid). The obvious asset of this functional form is that it preserves the relative simplicity of the coupling of harmonics imposed by the Coriolis term. This type of flow is known in the astrophysical literature as *shellular* differential rotation (Zahn 1992). It originates from a simple description of the baroclinic flow (the thermal wind in geophysics), which arises in stably stratified radiative zones of rotating stars (see, e.g., Rieutord 2006). The rotation is assumed to be uniform on spheres as a consequence of some shear-induced turbulence, which erases latitudinal gradients of the velocity (Zahn 1992). Low-frequency perturbations of such flows are driven by the combined effects of the Coriolis acceleration and buoyancy. Assuming differential rotation along the radial direction therefore comes to neglecting the effects of buoyancy on the fluid perturbations. Our model approaches this astrophysical configuration in the limit of weak stratification, when the Brunt-Väisälä frequency is small compared to the Coriolis frequency. When this is the case, some modes, called H1 in Dintrans *et al.* (1999), are essentially inertial modes slightly perturbed by buoyancy (i.e., the Coriolis acceleration is the main restoring force). In addition to giving a first look at the effect of differential rotation on inertial oscillations, shellular rotation may also provide a (partial) view on the properties of waves propagating in radiative zones inside rotating stars.

To complement the study of shellular flows, which may mimic stellar baroclinic flows, we also consider differential rotation associated with a barotropic fluid model. In this case, differential rotation only depends on the cylindrical radial coordinate $s = r \sin \theta$. Cylindrical differential rotation is expected in the convective zones of rapidly rotating stars or giant planets. It has been much investigated in the context of the Taylor-Couette instability, but in cylindrical geometry. However, recent experimental work by Kelley *et al.* (2007, 2010) and Rieutord *et al.* (2012) has raised the question of how the properties of inertial waves in spherical geometry are changed by the inclusion of cylindrical rotation. Since spherical geometry combined with cylindrical rotation results in the variables non-separability, which is a necessary condition for the existence of singularities like attractors, some properties of the perturbations can be derived by the sole analysis of the dynamics of characteristics.

This paper is organized as follows. Our physical model is described in § 2. The ideal case of an inviscid differentially rotating fluid is first examined in § 3 through a linear analysis in the short-wavelength approximation. Cylindrical and shellular rotation profiles are considered in § 3.1 and 3.2, respectively. A detailed study of the dynamics of characteristics allows us to determine the range of frequencies at which inertial oscillations may exist in differentially rotating fluids. The presence of turning surfaces, critical latitudes, and corotation resonances within the fluid is investigated. The full problem of a viscously rotating fluid is then investigated in § 4 with (linear) numerical calculations. Again, results with cylindrical and shellular rotation profiles are presented. Shear layers are shown to closely follow the attractors of characteristics obtained for an inviscid fluid in the short-wavelength approximation. Our simulations primarily focus on axisymmetric modes (§ 4.2), but a few examples of non-axisymmetric modes with a corotation resonance are also examined (§ 4.3). Concluding remarks and future directions are drawn in § 5.

2. Inertial modes in a differentially rotating shell: physical model

We consider a differentially rotating viscous fluid inside a spherical shell, located between radii ηR and R ($0 < \eta < 1$). The fluid is assumed to be homogeneous, incompressible, and of constant kinematic viscosity ν . We denote by \mathbf{u} the fluid's velocity. Any quantity x is decomposed as $x = x_0 + x_1$, where x_0 describes an unperturbed background

quantity and x_1 the associated disturbance ($|x_1| \ll |x_0|$). In an inertial frame, and using the set of spherical coordinates (r, θ, φ) , the linearized Navier-Stokes equation reads

$$\frac{\partial \mathbf{u}_1}{\partial t} + \Omega_0 \frac{\partial \mathbf{u}_1}{\partial \varphi} + 2\Omega_0 \mathbf{e}_z \times \mathbf{u}_1 + A(\mathbf{u}_1) \mathbf{e}_\varphi = -\nabla p_1 + \nu \Delta \mathbf{u}_1, \quad (2.1)$$

with $\Omega_0 = u_0^\varphi / r \sin \theta$ the fluid's angular velocity, $u_0^\varphi = \mathbf{u}_0 \cdot \mathbf{e}_\varphi$, $\mathbf{e}_z = \cos \theta \mathbf{e}_r - \sin \theta \mathbf{e}_\theta$ is the unit vector along the rotation axis, and p_1 denotes the pressure perturbation divided by the reference density. Since the fluid is incompressible, the linearized continuity equation reads

$$\nabla \cdot \mathbf{u}_1 = 0. \quad (2.2)$$

In Eq. (2.1), $A(\mathbf{u}_1)$ is proportional to the shear in the background flow:

$$A(\mathbf{u}_1) = r \sin \theta \mathbf{u}_1 \cdot \nabla \Omega_0. \quad (2.3)$$

In the following we consider either

- A cylindrical rotation profile, $\Omega_0 = \Omega_0(s)$, with $s = r \sin \theta$ the radial cylindrical coordinate. This rotation profile satisfies the Proudman-Taylor theorem for an incompressible homogeneous fluid in the inviscid limit, and no additional body-force needs to be assumed to ensure an equilibrium state for the differentially rotating background flow.

- A shellular rotation profile, $\Omega_0 = \Omega_0(r)$. In this case, differential rotation is assumed to be maintained by some appropriate body-force \mathbf{f} (arising for instance from Reynolds stresses or from a latitudinal entropy gradient), not included in our model. This body-force should verify $\nabla \times \mathbf{f} = -s \partial \Omega_0^2 / \partial z \mathbf{e}_\varphi$ for Taylor-Proudman theorem to be satisfied in this case.

We seek solutions to Eqs. (2.1) and (2.2) in the form $\exp(i\Omega_p t + im\varphi)$, where Ω_p denotes the wave angular frequency in the inertial frame. We introduce the Ekman number $E = \nu / R^2 \Omega_{\text{ref}}$, where the reference angular frequency, Ω_{ref} , refers to $\Omega_0(R)$ for shellular rotation or to $\Omega_0(s=0)$ for cylindrical rotation. Dropping all subscripts and taking the curl of Eq. (2.1), we are to solve:

$$\begin{cases} \nabla \times (i\tilde{\Omega}_p \mathbf{u} + 2\Omega \mathbf{e}_z \times \mathbf{u} + r \sin \theta (\mathbf{u} \cdot \nabla \Omega) \mathbf{e}_\varphi) = E \nabla \times \Delta \mathbf{u} \\ \nabla \cdot \mathbf{u} = 0, \end{cases} \quad (2.4)$$

where $\tilde{\Omega}_p = \Omega_p + m\Omega$ is the Doppler-shifted wave frequency (that is, the wave frequency in the frame rotating with the fluid).

We complete Eqs. (2.4) with stress-free boundary conditions at both boundaries: $\mathbf{u} \cdot \mathbf{e}_r = 0$ and $\mathbf{e}_r \times [\sigma] \mathbf{e}_r = \mathbf{0}$, where $[\sigma]$ denotes the viscous stress tensor. As discussed in Rieutord & Valdettaro (2010), the general properties of oscillation modes are essentially unchanged by the choice of boundary conditions. We thus opt for stress-free boundaries, which are numerically less demanding.

3. Inviscid problem: paths of characteristics, existence of turning surfaces and corotation resonances

Before examining the full solutions to Eqs. (2.4) by means of numerical simulations, we first study the inviscid limit and especially the dynamics of characteristics, which is known to feature the eigenfunctions of the viscous problem. For this purpose, we shall use cylindrical coordinates (s, φ, z) , and eliminate the velocity perturbations in favor of the pressure perturbations (p). The partial differential equation (PDE) satisfied by p is given in the appendix by Eq. (A 6). Retaining only the second-order terms, Eq. (A 6) becomes:

$$\frac{\partial^2 p}{\partial s^2} + \frac{A_z}{\tilde{\Omega}_p^2} \frac{\partial^2 p}{\partial s \partial z} + \left(1 - \frac{A_s}{\tilde{\Omega}_p^2}\right) \frac{\partial^2 p}{\partial z^2} = 0, \quad (3.1)$$

where

$$A_s = \frac{2\Omega}{s} \frac{\partial}{\partial s} (s^2\Omega) \quad \text{and} \quad A_z = \frac{2\Omega}{s} \frac{\partial}{\partial z} (s^2\Omega). \quad (3.2)$$

Eq. (3.1) matches equation (A 16) of Ogilvie (2005) for an homogeneous incompressible fluid. The equation governing the paths of characteristics in a meridional plane then reads

$$\frac{dz}{ds} = \frac{1}{2\tilde{\Omega}_p^2} \left(A_z \pm \xi^{1/2} \right) \quad \text{with} \quad \xi(s, z) = A_z^2 + 4\tilde{\Omega}_p^2 (A_s - \tilde{\Omega}_p^2). \quad (3.3)$$

For solid-body rotation, $A_z = 0$, $A_s = 4\Omega^2$, and Eq. (3.1) reduces to the well-known Poincaré equation for inertial waves. In this case, characteristics form straight lines in a meridional plane, and the fact that ξ is constant makes the entire shell either hyperbolic or elliptic for inertial waves. With differential rotation, however, the dependence of A_s , A_z and Ω with s and z implies that characteristics no longer form straight lines, as will be illustrated in the following. Also, ξ may vanish and change sign inside the shell. This makes possible the co-existence of hyperbolic and elliptic domains for pure inertial waves in a differentially rotating spherical shell, separated by turning surfaces. It is reminiscent of the existence of turning surfaces for gravito-inertial waves and magneto-inertial waves in rigidly rotating spherical shells, for which the perturbed pressure also satisfies a second-order PDE of mixed type in the inviscid limit (Friedlander & Siegmann 1982; Friedlander 1982, 1987; Dintrans *et al.* 1999). Equation (3.3) also shows that, in contrast to solid-body rotation, paths of characteristics with differential rotation depend on the azimuthal wavenumber m through $\tilde{\Omega}_p$. In the rest of this section, we study in more detail the dynamics of characteristics based on Eq. (3.3), considering a particular profile of cylindrical rotation in § 3.1, and of shellular rotation in § 3.2.

3.1. Cylindrical rotation

3.1.1. Paths of characteristics

To restrict the differential rotation function space to a one-parameter space, we consider the following background rotation profile:

$$\Omega(s)/\Omega_{\text{ref}} = 1 + \varepsilon(s/R)^2, \quad (3.4)$$

with $\Omega_{\text{ref}} = \Omega(s=0)$ the shell's angular frequency at the rotation axis, and where $|\varepsilon|$ can be seen as a Rossby number for the fluid. Eq. (3.1) then takes the form:

$$\frac{\partial^2 p}{\partial s^2} + \left(1 - \frac{A_s}{\tilde{\Omega}_p^2} \right) \frac{\partial^2 p}{\partial z^2} = 0, \quad (3.5)$$

where

$$\tilde{\Omega}_p(s) = \Omega_p + m\Omega(s) \quad (3.6)$$

is the Doppler-shifted frequency, and

$$A_s(s) = 4\Omega^2(s) \times \left[1 + \frac{\varepsilon(s/R)^2}{1 + \varepsilon(s/R)^2} \right]. \quad (3.7)$$

We will take $\varepsilon > -1/2$ so that $A_s > 0 \forall s \in [0, R]$ (Rayleigh's stability criterion). We will denote the quantity A_s by κ_s^2 (it is known as the square of the radial epicyclic frequency in astrophysical discs). We point out that Eq. (3.5) is symmetric by $z \rightarrow -z$, so that only positive values of z will be considered. From Eq. (3.3), paths of characteristics satisfy

$$\frac{dz}{ds} = \pm \xi^{1/2}, \quad (3.8)$$

with

$$\xi(s) = \frac{\kappa_s^2(s)}{\tilde{\Omega}_p^2(s)} - 1. \quad (3.9)$$

3.1.2. Existence of turning surfaces: D and DT inertial modes

The relation $\xi(s) = 0$ defines turning surfaces that separate the hyperbolic and elliptic domains. They correspond to cylinders in a meridional slice of the shell. Their location satisfies

$$\tilde{\Omega}_p^2(s) = \kappa_s^2(s), \quad (3.10)$$

with waves propagating when $\kappa_s^2(s) \geq \tilde{\Omega}_p^2(s)$. Here and in the following, we will assume that the hyperbolic domains of the spherical shell, where ξ is positive, host inertial modes of oscillations. The dependence of ξ on s leads to two kinds of inertial modes with cylindrical rotation:

- (i) modes that exhibit at least one turning surface within the shell, which we call DT modes for future reference (D for differential rotation, and T for turning surface),
- (ii) generalized inertial modes with no turning surfaces within the shell, which we name D modes.

The occurrence of axisymmetric ($m = 0$) and of some non-axisymmetric D and DT modes is illustrated in Fig. 1. In all panels, the mode's eigenfrequency in the inertial frame (Ω_p) is shown in x-axis, and the differential rotation parameter ε is in y-axis. Contours are obtained by numerically calculating the right-hand side of Eq. (3.9). DT modes, which are represented by white areas, have $\xi < 0$ at least once within the shell. D modes satisfy $\xi \geq 0$ everywhere in the shell and are shown by the blue area. No inertial modes can propagate if $\xi < 0$ in the entire shell, such case being depicted in red. Note that axisymmetric inertial waves may propagate for eigenfrequencies $\Omega_p > 2\Omega_{\text{ref}}$ if $\varepsilon > 0$ (see top-left panel in Fig. 1). Note also that the results shown in Fig. 1 are independent of the shell's aspect ratio η , as is actually the dynamics of characteristics with our cylindrical rotation profile.

The transition curves that separate D and DT modes satisfy $\xi(s = 0) = 0$ and $\xi(s = R) = 0$. The solution to $\xi(s) = 0$ can be cast as $\Omega_p/\Omega_{\text{ref}} = -m[1 + \varepsilon(s/R)^2] \pm 2\sqrt{[1 + 2\varepsilon(s/R)^2][1 + \varepsilon(s/R)^2]}$. Applied to the following cases:

- $\xi(s = 0) = 0$, that is when the turning surface matches the location of the rotation axis, we have

$$\Omega_p/\Omega_{\text{ref}} = -m \pm 2, \quad (3.11)$$

such case being depicted by vertical dotted lines in Fig. 1,

- $\xi(s = R) = 0$, when the turning surface passes by the shell's surface, yields

$$\Omega_p/\Omega_{\text{ref}} = -m(1 + \varepsilon) \pm 2\sqrt{(1 + 2\varepsilon)(1 + \varepsilon)}, \quad (3.12)$$

which is overplotted by solid curves in Fig. 1.

We point out that there may exist two turning surfaces in a meridional plane. This occurs for instance for the DT modes with $m = 4$ located in the (small) region of parameter space below the solid curve near $\Omega_p = -2\Omega_{\text{ref}}$ and $\varepsilon = -0.5$.

Non-axisymmetric modes may feature a corotation resonance within the shell when $\tilde{\Omega}_p(s) = 0$. The location of such *critical cylinders* is given by

$$s_{\text{crit}} = R \sqrt{\varepsilon^{-1} \times \left(-1 - \frac{\Omega_p}{m\Omega_{\text{ref}}} \right)}. \quad (3.13)$$

For $m > 0$, modes with $\varepsilon \leq 0$ have a critical layer if $-m \leq \Omega_p/\Omega_{\text{ref}} \leq -m(1 + \varepsilon)$, and those with $\varepsilon \geq 0$ if $-m(1 + \varepsilon) \leq \Omega_p/\Omega_{\text{ref}} \leq -m$. Modes that exhibit a critical cylinder within the shell are located between the two orange solid curves in Fig. 1.

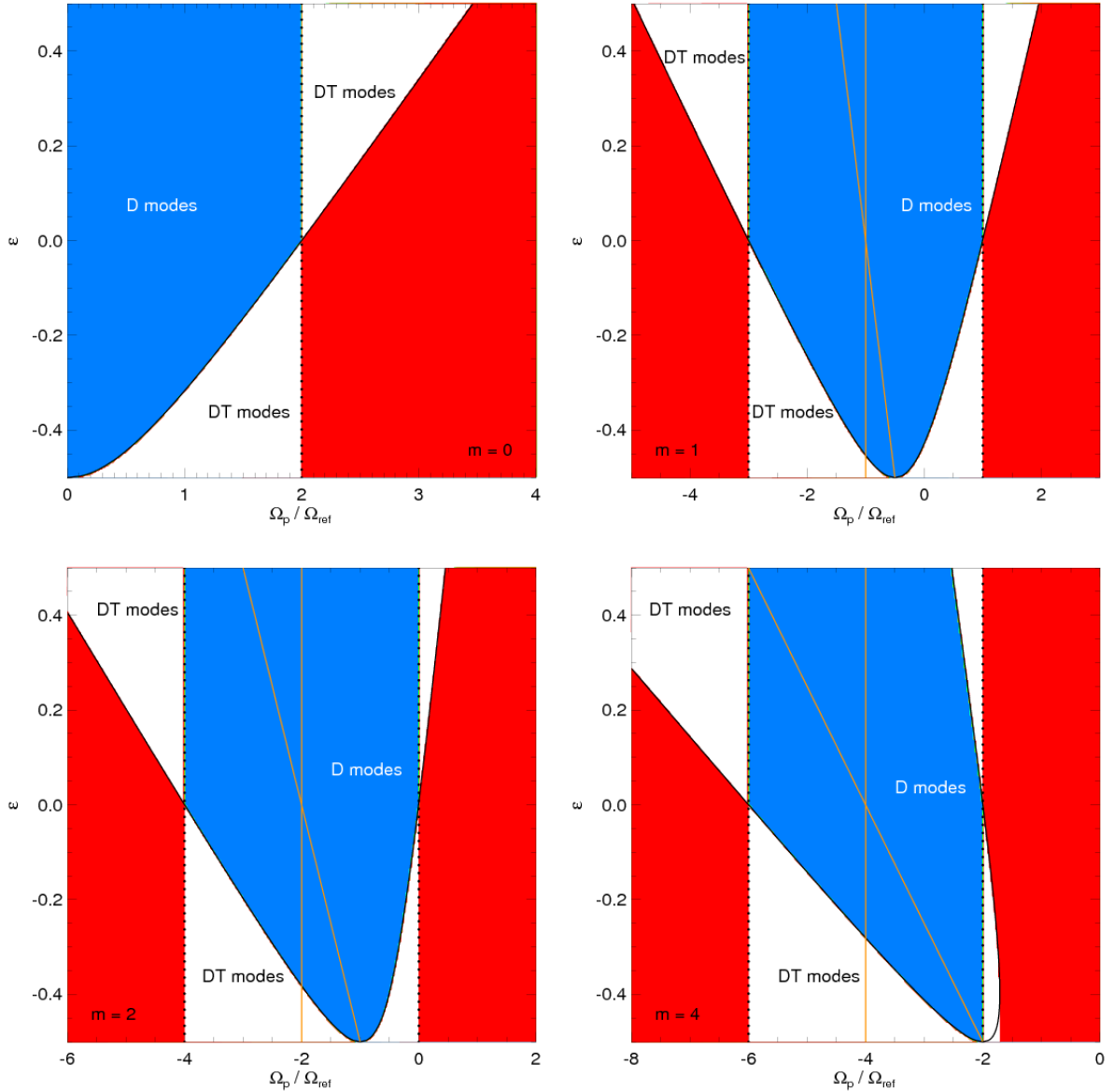


FIGURE 1. Illustration of the two kinds of inertial modes propagating in a differentially rotating fluid, with cylindrical rotation profile $\Omega(s)/\Omega_{\text{ref}} = 1 + \varepsilon(s/R)^2$ (Ω_{ref} denotes the shell's angular frequency at the rotation axis). Results are shown for azimuthal wavenumbers m equal to 0, 1, 2 and 4 from top-left to bottom-right. DT modes, represented by white areas, exhibit turning surfaces inside the shell. D modes correspond to the blue area and do not feature turning surfaces inside the shell. No inertial modes may propagate in the red areas. The solutions to $\xi(s=0) = 0$ are shown by vertical dotted lines, and the solutions to $\xi(s=R) = 0$ by solid black curves. Non-axisymmetric modes that feature a critical cylinder inside the shell (corotation resonance) are located between the two orange solid curves.

The minimum and maximum frequencies at which inertial waves may propagate in a shell with cylindrical rotation is summarized in Fig. 2 for the four azimuthal wavenumbers considered in Fig. 1. These frequencies are obtained by solving $\xi(s) = 0$. They correspond to the minimum and maximum frequencies amongst the four values given by Eqs. (3.11) and (3.12), except for $m = 4$ and ε approaching -0.5 (in which case, as already pointed out before, there are two turning surfaces inside the shell). Fig. 2 highlights that the range of eigenfrequencies at which inertial modes of oscillations may exist in a spherical shell is broader with cylindrical rotation than with solid rotation, particularly *if* the rotation

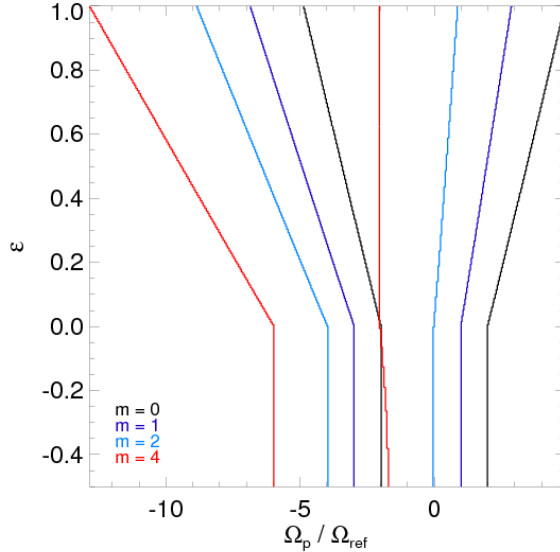


FIGURE 2. Range of eigenfrequencies (Ω_p , x-axis) for inertial modes of oscillations in a rotating shell with cylindrical rotation profile $\Omega(s)/\Omega_{\text{ref}} = 1 + \varepsilon(s/R)^2$. Eigenfrequencies are in units of Ω_{ref} , the shell's angular frequency at the rotation axis. Results are for $m = 0, 1, 2$ and 4 . For a given m , the minimum and maximum frequencies at which inertial modes exist correspond to the left and right curves, respectively.

profile is an increasing function of the cylindrical radial coordinate. This is expected, because of the larger frequencies at which the fluid may rotate in this case.

3.1.3. Dispersion relation, phase and group velocities

We examine in this paragraph the propagation properties of local waves in a meridional plane. In the short-wavelength approximation, the general expressions for the wave dispersion relation, the phase and group velocities are given in the Appendix by Eqs. (A 7), (A 9) and (A 10). For our cylindrical rotation profile, Eq. (A 7) reduces to

$$\tilde{\Omega}_p^2(s) = \kappa_s^2(s) \frac{k_z^2}{\|\mathbf{k}\|^2}, \quad (3.14)$$

where $\|\mathbf{k}\| = \sqrt{k_s^2 + k_z^2}$. In the frame rotating with the fluid, the phase velocity, $\mathbf{v}_p = \tilde{\Omega}_p \mathbf{k} / \|\mathbf{k}\|^2$, satisfies

$$\mathbf{v}_p = \pm \kappa_s(s) \frac{k_z \mathbf{k}}{\|\mathbf{k}\|^3}, \quad (3.15)$$

while the group velocity, $\mathbf{v}_g = \partial \tilde{\Omega}_p / \partial \mathbf{k}$, is given by

$$\mathbf{v}_g = \pm \kappa_s(s) \frac{k_s}{\|\mathbf{k}\|^3} (-k_z \mathbf{e}_s + k_s \mathbf{e}_z). \quad (3.16)$$

From Eqs. (3.9) and (3.14), $k_s = 0$ at a turning surface (where ξ vanishes). At this location, the radial component of the phase velocity therefore vanishes, as well as the two other components of the group velocity (that is, rays are perpendicular to the turning surface).

A corotation resonance occurs inside the shell where $\tilde{\Omega}_p(s) = 0$. This formally happens if $|k_s| \rightarrow \infty$, in which case the modulus of the phase velocity and the group velocity both tend to zero, or if $k_z \rightarrow 0$, in which case the phase velocity cancels out while the radial component of the group velocity cancels out. In both cases, characteristics become more and more parallel to the rotation axis as they approach the corotation resonance (their slope $|dz/ds|$ increases), and they do not cross corotation (as the radial component of the group velocity tends to zero at this location). The fact that the phase velocity progressively

decreases to zero upon approaching corotation suggests that non-linear effects should become important near this location, as pointed out for instance by Barker & Ogilvie (2010) for internal gravity waves in a background shear flow, which satisfy a dispersion relation similar to that in Eq. (3.14) with the epicyclic frequency squared κ_s^2 replaced by the Brunt-Väisälä frequency squared.

3.2. Shellular rotation

We now come to the propagation properties of inertial modes of oscillation in fluids with shellular rotation (the background rotation profile being a prescribed function of the spherical radius). As in the case of cylindrical rotation, we show in this section that two kinds of inertial modes can be distinguished, based on the presence or not of turning surfaces within the shell. We then discuss the range of eigenfrequencies at which inertial modes may exist, the existence of critical latitudes and corotation resonances.

3.2.1. D and DT inertial modes

We adopt the same strategy as in § 3.1 for cylindrical rotation and restrict the differential rotation function space to a one-parameter space. We take the following shellular rotation profile:

$$\Omega(r) = \Omega_{\text{ref}} \times (r/R)^\sigma, \quad (3.17)$$

where $r = \sqrt{s^2 + z^2}$, $\Omega_{\text{ref}} = \Omega(r = R)$ is the angular frequency at the shell's surface, and $\sigma > -2$ to avoid centrifugal instabilities (Rayleigh's stability criterion, $A_s > 0$, is satisfied). The quantity $|1 - \eta^\sigma|$, which measures the relative difference of angular frequencies between the inner core and the shell's surface, can be seen as a Rossby number for the fluid. Eq. (3.1) being symmetric by $z \rightarrow -z$ for shellular rotation profile, only positive values of z will be considered (as with cylindrical rotation). From Eq. (3.3), paths of characteristics satisfy

$$\frac{dz}{ds} = A(r) \frac{sz}{R^2} \pm \xi^{1/2}, \quad (3.18)$$

where

$$\xi(s, z) = A^2(r) \frac{s^2 z^2}{R^2} + 2A(r) \frac{s^2}{R^2} + \frac{4\Omega^2(r) - \tilde{\Omega}_p^2(r)}{\tilde{\Omega}_p^2(r)}, \quad (3.19)$$

$$A(r) = \sigma \frac{R^2}{r^2} \frac{\Omega^2(r)}{\tilde{\Omega}_p^2(r)}, \quad (3.20)$$

and $\tilde{\Omega}_p(r) = \Omega_p + m\Omega(r)$ is the Doppler-shifted wave frequency. Whenever paths of characteristics are calculated by solving Eq. (3.18) (or Eq. (3.8) for cylindrical rotation), reflections are imposed at the shell's inner core ($r = \eta R$) and surface ($r = R$), at the rotation ($s = 0$) and equatorial ($z = 0$) axes, and at the location of turning surfaces (where $\xi = 0$).

The possibility that ξ vanishes within the shell leads again to two kinds of inertial modes with shellular rotation: DT modes, with at least one turning surface inside the shell, and D modes, with no turning surfaces inside the shell. The occurrence of axisymmetric and of some non-axisymmetric D and DT modes is depicted in Fig. 3. Contours are obtained upon calculation of Eq. (3.19) in a spherical shell with $\eta = 0.35$. As in Fig. 1, D and DT modes are depicted by blue and white areas, respectively, and no inertial modes exist in the red areas.

The relation $\xi = 0$ defines turning surfaces with colatitude $\theta(r)$ given by

$$\sin^2 \theta(r) = \frac{1}{2} \left[1 + \frac{2\tilde{\Omega}_p^2(r)}{\sigma\Omega^2(r)} \pm \mu^{1/2}(r) \right], \quad (3.21)$$

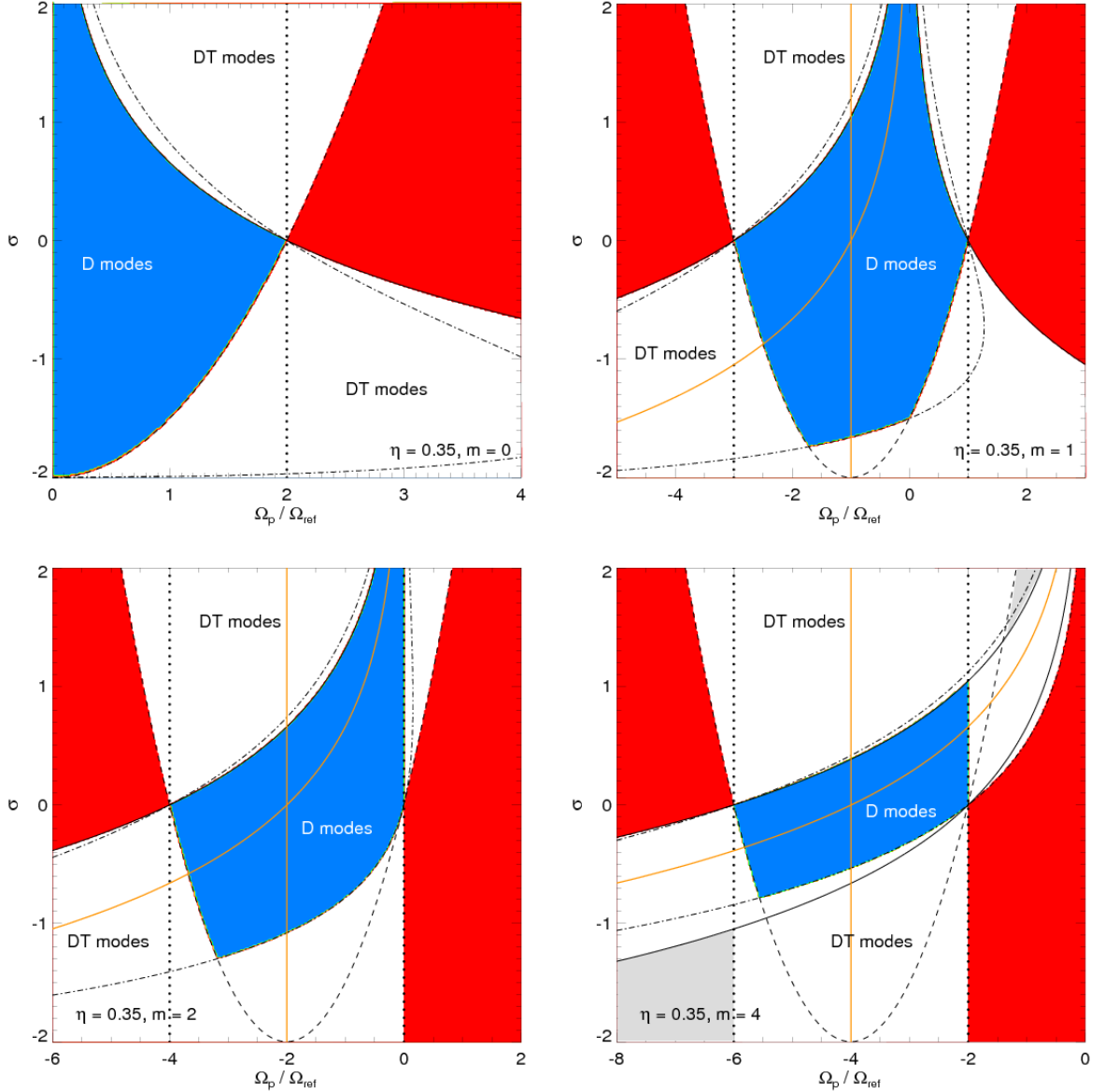


FIGURE 3. Occurrence of D and DT inertial modes with the shellular rotation profile $\Omega(r)/\Omega_{\text{ref}} = (r/R)^\sigma$ (Ω_{ref} denotes the angular frequency at the shell's surface). Results are obtained for $\eta = 0.35$, and $m = 0, 1, 2$ and 4 from top-left to bottom-right. DT modes (white areas) have at least one turning surface inside the shell. D modes (blue area) do not have turning surfaces. No inertial modes exist within the red areas. The dotted, dashed, solid and dash-dotted curves are solutions to Eqs. (3.23) to (3.26), respectively. In the bottom-right panel, grey areas depict DT modes located between two turning surfaces that englobe the shell's inner core and surface. For $m \neq 0$, modes that feature a critical layer inside the shell (where $\tilde{\Omega}_p(r) = 0$) are located between the two orange solid curves.

with

$$\mu(r) = 1 + \frac{4(4 + \sigma)\tilde{\Omega}_p^2(r)}{\sigma^2\Omega^2(r)}. \quad (3.22)$$

Another way to find the occurrence of DT modes is to require that, for given values of m , Ω_p and σ , the inequality $0 \leq \sin^2 \theta(r) \leq 1$ is satisfied at least once within the shell. We also point out that the two propositions $\forall \{s, z\}, \xi(s, z) > 0$, and $\forall r, |\tilde{\Omega}_p(r)| < 2\Omega(r)$, seem to be equivalent numerically (as we have checked). In other words, if the whole shell satisfies the condition for hyperbolicity, it also meets the standard criterion for propagation

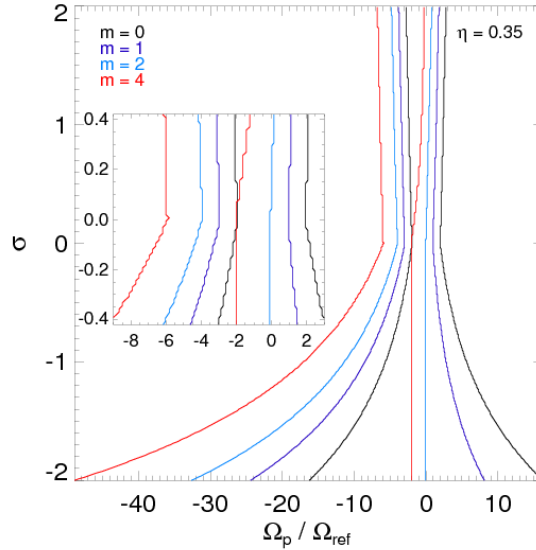


FIGURE 4. Minimum and maximum eigenfrequencies (x-axis) at which inertial modes of oscillation may exist with shellular rotation profile $\Omega(r)/\Omega_{\text{ref}} = (r/R)^\sigma$, for $m = 0, 1, 2$ and 4 ($\eta = 0.35$). Eigenfrequencies are in units of the angular frequency at the shell's surface. The inset plot focuses on previous range of eigenfrequencies for $\sigma \in [-0.4, 0.4]$.

of inertial waves everywhere locally. Thus, regions with no mode propagation, and those with D modes, can be distinguished by requiring that D modes verify $|\tilde{\Omega}_p(r)| < 2\Omega(r)$ in the whole shell.

The transition curves that separate D and DT modes then satisfy:

- $\sin^2 \theta(R) = 0$, when the turning surface hits the shell's surface at colatitude $\theta = 0$.

It reads $|\tilde{\Omega}_p(R)| = 2\Omega(R)$, or

$$\Omega_p/\Omega_{\text{ref}} = -m \pm 2, \quad (3.23)$$

expression that is depicted by vertical dotted lines in Fig. 3.

- $\sin^2 \theta(R) = 1$, which yields

$$\Omega_p/\Omega_{\text{ref}} = -m \pm \sqrt{2(2 + \sigma)}, \quad (3.24)$$

which is overplotted by a dashed curve.

- $\sin^2 \theta(\eta R) = 0$, which can be recast as

$$\begin{cases} \Omega_p/\Omega_{\text{ref}} = (2 - m)\eta^\sigma & \text{if } \Omega_p/(2 - m) > 0 \\ \Omega_p/\Omega_{\text{ref}} = -(2 + m)\eta^\sigma & \text{if } \Omega_p/(2 + m) < 0, \end{cases} \quad (3.25)$$

and are shown by solid lines.

- $\sin^2 \theta(\eta R) = 1$, when the turning surface hits the shell's inner core at colatitude $\theta = \pi/2$, that is when

$$\Omega_p/\Omega_{\text{ref}} = \eta^\sigma \left(-m \pm 2\sqrt{1 + \sigma/2} \right), \quad (3.26)$$

expression that is shown by dash-dotted curves.

DT modes with $|m| \leq 2$ are located between the turning surface and the shell's surface for $\sigma > 0$ (since the background velocity increases with radius), and between the shell's inner core and the turning surface for $\sigma < 0$. A more complex situation arises when $|m| > 2$, where the equation $|\tilde{\Omega}_p(\eta R)| = 2\Omega(\eta R)$ may admit two solutions for a given Ω_p , as can be seen from Eq. (3.25). In the bottom-right panel of Fig. 3 ($m = 4$), DT

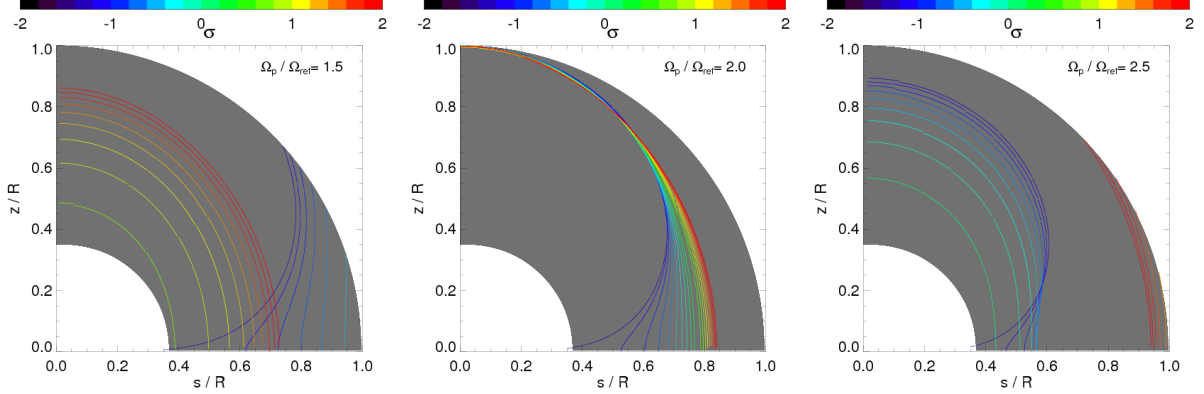


FIGURE 5. Location of turning surfaces for $m = 0$ modes with varying the power-law index of the shellular rotation profile, for $\Omega_p = 1.5\Omega_{\text{ref}}$ (left panel), $\Omega_p = 2\Omega_{\text{ref}}$ (middle panel), and $\Omega_p = 2.5\Omega_{\text{ref}}$ (right panel).

modes located between the two solid lines propagate between the shell's inner core and the turning surface, since as D modes they satisfy $|\tilde{\Omega}_p(\eta R)| < 2\Omega(\eta R)$. In contrast, the DT modes above the upper solid curve, and those below the lower solid curve, propagate between the turning surface and the shell's surface. Interestingly, modes with $|m| > 2$ may exhibit two turning surfaces that are located between the shell's inner core and the shell's surface. This brings the possibility of waves naturally bouncing between two turning surfaces without interacting with the shell's boundaries. Such modes are depicted by grey areas in the bottom-right panel in Fig. 3. Note, however, that this particular set of non-axisymmetric modes will necessarily feature a critical layer (corotation resonance) between both turning surfaces, where $\tilde{\Omega}_p$ vanishes. The location of such critical layers is given by $r = R(-\Omega_p/m\Omega_{\text{ref}})^{1/\sigma}$. For $m > 0$, modes with $\sigma \leq 0$ have a critical layer if $-m\eta^\sigma \leq \Omega_p/\Omega_{\text{ref}} \leq -m$, and those with $\sigma \geq 0$ if $-m \leq \Omega_p/\Omega_{\text{ref}} \leq -m\eta^\sigma$. Modes that exhibit a critical layer within the shell are located between the two orange solid curves in Fig. 3. They will be further discussed in Sections 3.2.3 and 4.3.2.

The range of eigenfrequencies Ω_p for which inertial modes of oscillation may exist in a spherical shell with $\eta = 0.35$ is displayed in Fig. 4 for $m = 0, 1, 2$, and 4. Compared to solid-body rotation, inertial modes with shellular rotation may exist at much larger frequencies, especially if the rotation profile is a decreasing function of radius.

Finally, the location of turning surfaces, given by Eq. (3.21), is depicted in a meridional slice in Fig. 5 for $m = 0$ modes with σ ranging from -2 to 2, and increasing by 0.2. Results are shown for $\Omega_p/\Omega_{\text{ref}} = 1.5, 2$, and 2.5 from left to right. For $\Omega_p = 2\Omega_{\text{ref}}$, turning surfaces exist for all values of σ but for $\sigma = 0$ (corresponding to solid-body rotation; note however that turning surfaces exist in the limit $|\sigma| \rightarrow 0$). In all three panels, DT modes with $\sigma < 0$ exist between the shell's inner core and the turning surface (they may therefore exist without reflexions on the shell's surface). Similarly, DT modes with $\sigma > 0$ exist between the turning surface and the shell's surface, and may therefore exist without reflexions on the shell's inner core. This case will be illustrated in Section 4.2.2, where we will show that DT modes may feature shear layers following attractors of characteristics in the absence of an inner core (the necessary reflexion being provided by the shell's surface and the turning surface).

3.2.2. Critical latitudes

Rays tangent to the shell's inner core define a critical latitude θ_i . They satisfy $dz/ds = -s/z$ with $\eta R = \sqrt{s^2 + z^2}$. Combining Eqs. (3.18) to (3.20), rays intersect the shell's inner core at $s = s_c$, with

$$s_c = \eta R \left(1 - \frac{\tilde{\Omega}_p^2(\eta R)}{4\Omega^2(\eta R)} \right)^{1/2}. \quad (3.27)$$

A critical latitude θ_i at the shell's inner core therefore exists for modes with $|\tilde{\Omega}_p(\eta R)| \leq 2\Omega(\eta R)$, and verifies

$$\sin \theta_i = \frac{\tilde{\Omega}_p(\eta R)}{2\Omega(\eta R)}, \quad (3.28)$$

which is a straightforward generalization of the expression for solid-body rotation. For fixed values of η , m and Ω_p , and for $\sigma > 0$, $\sin \theta_i \rightarrow 1$ as σ increases. For $\sigma < 0$, $\sin \theta_i \rightarrow 0$ as $|\sigma|$ increases.

Similarly, it is easy to show that a critical latitude θ_o exists at the shell's surface for those modes that satisfy $|\tilde{\Omega}_p(R)| \leq 2\Omega(R)$, with expression given by

$$\sin \theta_o = \frac{\tilde{\Omega}_p(R)}{2\Omega(R)}, \quad (3.29)$$

independently of σ . The outer critical latitude has therefore the same value as in the solid-body rotation case.

Critical latitudes also exist with cylindrical rotation. For our cylindrical rotation profile, an inner critical latitude exists if $\xi(s)$, given by Eq. (3.9), is positive for $s \in [0, \eta R]$. Similarly, an outer critical latitude exists if $\xi \geq 0 \forall s \in [0, R]$ (that is, for D modes only). There is, however, no simple expressions for the inner and outer critical latitudes with our cylindrical rotation profile.

3.2.3. Dispersion relation, phase and group velocities

In the short-wavelength approximation, the wave dispersion relation given by Eq. (A 7) becomes

$$\tilde{\Omega}_p^2(r) = 4\Omega^2(r) \frac{k_z^2}{\|\mathbf{k}\|^2} \times \left[1 + \frac{\sigma s^2}{2 r^2} \left(1 - \frac{z k_s}{s k_z} \right) \right] \quad (3.30)$$

for our shellular rotation profile, with $\|\mathbf{k}\| = \sqrt{k_s^2 + k_z^2}$. We see that the bracket term in the above equation can be negative: inertial waves may become unstable for shellular rotation. As discussed in the appendix, this is a form of the Goldreich-Schubert-Fricke instability in the limit of an inviscid incompressible fluid (Goldreich & Schubert 1967; Fricke 1968). In that limit, Eq. (A 7) indicates that the instability can in principle occur whenever $\partial\Omega/\partial z \neq 0$ (or, equivalently, when $A_z \neq 0$). Assuming that inertial waves remain stable against our shellular rotation profile, we introduce

$$\mathcal{B} = \left[1 + \frac{\sigma s^2}{2 r^2} \left(1 - \frac{z k_s}{s k_z} \right) \right]^{1/2}, \quad (3.31)$$

and Eq. (3.30) reduces to $\tilde{\Omega}_p(r) = \pm 2\mathcal{B}\Omega(r)|k_z|/\|\mathbf{k}\|$. Note that $\mathcal{B} = 1$ for solid-body rotation. In the rotating frame, the phase velocity reads

$$\mathbf{v}_p = \pm 2\mathcal{B}\Omega(r) \frac{k_z \mathbf{k}}{\|\mathbf{k}\|^3}, \quad (3.32)$$

and the group velocity is given by

$$\mathbf{v}_g = \pm 2\Omega(r) \frac{k_s}{\|\mathbf{k}\|^3} (-k_z \mathbf{e}_s + k_s \mathbf{e}_z) \times \left[\mathcal{B} + \frac{\sigma s z \|\mathbf{k}\|^2}{4 r^2 k_s k_z} \mathcal{B}^{-1} \right]. \quad (3.33)$$

We now examine the case where a critical layer forms inside the shell, where $\tilde{\Omega}_p(r) = 0$. Inspection of Eq. (3.30) shows that there are formally three cases where $\tilde{\Omega}_p(r)$ may vanish:

- $k_s \rightarrow \infty$ at finite k_z . In this case, $\mathbf{v}_p = \mathbf{0}$ and $\mathbf{v}_g = \mathbf{0}$ at corotation, which is similar to the behavior obtained with cylindrical rotation (inertial waves do not cross corotation in such case).

- $k_z \rightarrow 0$ at finite k_s , in which case $\mathbf{v}_p = \mathbf{0}$, $\mathbf{v}_g \cdot \mathbf{e}_s = 0$, and $|\mathbf{v}_g \cdot \mathbf{e}_z| \rightarrow \infty$. Surprisingly, this case indicates that inertial waves may propagate across a critical layer (with locally vertical paths of characteristics).

- $\mathcal{B} \rightarrow 0$, which implies that $\mathbf{v}_p = \mathbf{0}$, $|\mathbf{v}_g \cdot \mathbf{e}_s| \rightarrow \infty$ and $|\mathbf{v}_g \cdot \mathbf{e}_z| \rightarrow \infty$. This case also formally shows that inertial waves may cross a critical layer. The condition $\mathcal{B} = 0$ can be recast as

$$\left. \frac{dz}{ds} \right|_{\text{crit}} \equiv - \left. \frac{k_s}{k_z} \right|_{\hat{\Omega}_p(r)=0} = - \frac{s}{z} \left(1 + \frac{2r^2}{\sigma s^2} \right), \quad (3.34)$$

which shows that, if $\mathcal{B} = 0$ at corotation, then paths of characteristics have a finite slope upon crossing the critical layer.

The propagation properties of inertial waves in viscous fluids with a critical layer will be examined in Section 4.3.2 with the results of numerical calculations. We stress again that the fact the phase speed vanishes at corotation indicates that non-linear effects should occur near this location, which are not captured by the present linear analysis, nor by the numerical solutions of Section 4.3.2.

4. Viscous problem: shear layers, behaviour at corotation resonances, comparison to inviscid analysis

We have described in Section 3 the propagation properties of inertial waves in a spherical shell with (specific) cylindrical and shellular rotation profiles. We have shown that in both cases, modes of oscillations satisfy in the inviscid limit a second-order PDE of mixed type. Two families of eigenmodes can therefore be distinguished: D modes, which may propagate throughout the entire shell (the hyperbolic domain covers the whole shell), and DT modes, which feature turning surfaces inside the shell (the hyperbolic domain covers part of the shell). Compared to solid-body rotation, the presence of turning surfaces with differential rotation tends to broaden the range of frequencies at which inertial waves may propagate in a spherical shell.

An interesting result from our analysis in Section 3 is that paths of characteristics depend on the azimuthal wavenumber m (through the space-varying Doppler-shifted frequency). In contrast to solid-body rotation, the structure of non-axisymmetric modes cannot be simply inferred from that of axisymmetric modes. However, as far as their dynamical properties are concerned, $m \neq 0$ and $m = 0$ modes only differ by the possible presence of corotation resonances for $m \neq 0$. We will therefore examine the general properties of viscous modes of oscillations for $m = 0$ modes only. This is done in Section 4.2, where we take the same rotation profiles as in Section 3. We show that the structure of shear layers in the viscous problem closely follows the paths of characteristics derived in the inviscid problem. We particularly focus on singular modes featuring a shear layer that converges towards a short-period attractor. Some of these singular modes form through reflexions at turning surfaces and may therefore exist in the absence of an inner core. A qualitative analysis of the occurrence of modes with quasi-periodic orbits of characteristics is also done at Section 4.2.3. We finally examine in Section 4.3 a few $m \neq 0$ viscous eigenmodes with corotation resonances.

4.1. Numerical method

Our numerical simulations solve the linearized differential system (2.4) and related stress-free boundary conditions, using a spectral approach. Fields are decomposed into spherical harmonics (see, e.g., Rieutord 1987), with the perturbed velocity expanded as

$$\mathbf{u}(r, \theta, \varphi) = \sum_{\ell=0}^{\infty} \sum_{m=-\ell}^{\ell} u_m^{\ell}(r) \mathbf{R}_{\ell}^m + v_m^{\ell}(r) \mathbf{S}_{\ell}^m + w_m^{\ell}(r) \mathbf{T}_{\ell}^m, \quad (4.1)$$

with $\mathbf{R}_{\ell}^m = Y_{\ell}^m(\theta, \varphi) \mathbf{e}_r$, $\mathbf{S}_{\ell}^m = \nabla Y_{\ell}^m$, and $\mathbf{T}_{\ell}^m = \nabla \times \mathbf{R}_{\ell}^m$, and where Y_{ℓ}^m denote the usual spherical harmonics normalized on the sphere of unit radius. In the radial direction,

equations are discretized on Gauss-Lobatto collocation nodes associated with Chebyshev polynomials. Equations are truncated at order L for the spherical harmonics basis, and at order N_r for the Chebyshev basis. The incomplete Arnoldi-Chebyshev algorithm is used to compute pairs of complex eigenvalues (Ω_p) and eigenvectors, given an initial guess value for Ω_p (for details on this numerical method, see Valdetaro *et al.* 2007). Values of N_r and L are mode-dependent, and will be specified below. Unless otherwise stated, all modes are calculated assuming symmetry with respect to the equatorial plane.

4.1.1. Shellular rotation

For the shellular rotation profile that we consider, $\Omega(r)/\Omega_{\text{ref}} = (r/R)^\sigma$, projecting Eqs. (2.4) onto $\mathbf{R}_\ell^{\mathbf{m}}$ and $\mathbf{T}_\ell^{\mathbf{m}}$ gives the following two equations:

$$\left. \begin{aligned} E\Delta_\ell w_m^\ell + \left[\frac{2im\Omega(r)}{\ell(\ell+1)} - i\tilde{\Omega}_p(r) \right] w_m^\ell = \\ -2\Omega(r) \left[A(\ell, m)r^{\ell-1} \frac{d(r^{2-\ell}u_m^{\ell-1})}{dr} + A(\ell+1, m)r^{-\ell-2} \frac{d(r^{\ell+3}u_m^{\ell+1})}{dr} \right] \\ + r \frac{d\Omega}{dr} [-(\ell+1)A(\ell+1, m)u_m^{\ell+1} + \ell A(\ell, m)u_m^{\ell-1}], \\ E\Delta_\ell \Delta_\ell (ru_m^\ell) + \left[\frac{2im\Omega(r)}{\ell(\ell+1)} - i\tilde{\Omega}_p(r) \right] \Delta_\ell (ru_m^\ell) = \\ 2\Omega(r) \left[B(\ell, m)r^{\ell-1} \frac{d(r^{1-\ell}w_m^{\ell-1})}{dr} + B(\ell+1, m)r^{-\ell-2} \frac{d(r^{\ell+2}w_m^{\ell+1})}{dr} \right] \\ - imr \frac{d^2\Omega}{dr^2} u_m^\ell - 2im \frac{d\Omega}{dr} (u_m^\ell + v_m^\ell) \\ + 2 \frac{d\Omega}{dr} [B(\ell, m)w_m^{\ell-1} + B(\ell+1, m)w_m^{\ell+1}], \end{aligned} \right\} \quad (4.2)$$

where

$$A(\ell, m) = \frac{1}{\ell^2} \left(\frac{\ell^2 - m^2}{4\ell^2 - 1} \right)^{1/2}, \quad B(\ell, m) = \ell^2(\ell^2 - 1)A(\ell, m), \quad \Delta_\ell = \frac{1}{r} \frac{d^2}{dr^2} r - \frac{\ell(\ell+1)}{r^2}.$$

In Eqs. (4.2), since the fluid is incompressible,

$$v_m^\ell = \frac{1}{\ell(\ell+1)r} \frac{d(r^2 u_m^\ell)}{dr}. \quad (4.3)$$

For solid-body rotation, $\Omega(r) = \Omega_{\text{ref}}$ and Eqs. (4.2) reduce to equations (2.2) of Rieutord & Valdetaro (1997) (note that these authors defined the Ekman number as $E = \nu/2R^2\Omega_{\text{ref}}$, while our definition does not include the factor 2). After projection on the spherical harmonics, stress-free boundary conditions read

$$u_m^\ell = \frac{d^2(ru_m^\ell)}{dr^2} = \frac{d}{dr} \left(\frac{w_m^\ell}{r} \right) = 0 \quad (4.4)$$

for the radial functions taken at $r = \eta R$ or $r = R$. Eqs. (4.2) to (4.4) can be recast as an eigenvalue problem featuring a tridiagonal block matrix, like for solid-body rotation. More details into the numerical scheme can be found in Rieutord & Valdetaro (1997).

4.1.2. Cylindrical rotation

For our cylindrical rotation profile, $\Omega(s)/\Omega_{\text{ref}} = 1 + \varepsilon(s/R)^2$, projecting Eqs. (2.4) onto \mathbf{R}_ℓ^m and \mathbf{T}_ℓ^m gives, after some tedious algebra, two long differential equations, which we do not write for the sake of legibility. The second-order differential equation satisfied by w_m^ℓ can be cast as a linear combination of $u_m^{\ell\pm 3}$, $du_m^{\ell\pm 3}/dr$, $u_m^{\ell\pm 1}$, $du_m^{\ell\pm 1}/dr$ and $w_m^{\ell\pm 2}$ (the term in front of $w_m^{\ell\pm 2}$ vanishes for $m = 0$). The fourth-order differential equation for u_m^ℓ exhibits terms in $w_m^{\ell\pm 3}$, $dw_m^{\ell\pm 3}/dr$, $w_m^{\ell\pm 1}$, $dw_m^{\ell\pm 1}/dr$, $u_m^{\ell\pm 2}$, $du_m^{\ell\pm 2}/dr$ and $d^2u_m^{\ell\pm 2}/dr^2$ (the terms in front of $u_m^{\ell\pm 2}$, $du_m^{\ell\pm 2}/dr$ and $d^2u_m^{\ell\pm 2}/dr^2$ vanish for $m = 0$). Along with stress-free boundary conditions, these equations take the form of an eigenvalue problem where the matrix to invert has blocks composed of (up to) seven bands. The coupling between harmonics of ranks ℓ , $\ell \pm 1$, $\ell \pm 2$ and $\ell \pm 3$ arises from our particular cylindrical profile.

4.2. Axisymmetric eigenmodes: a few illustrative cases

We present in this section the results of simulations for axisymmetric eigenmodes with moderate viscosity, the default Ekman number being $E = 10^{-8}$. Unless otherwise stated, our simulations are carried out with a shell's aspect ratio $\eta = 0.35$. The propagation properties of shear layers for weakly-damped eigenmodes is compared with the analytic description based on paths of characteristics, detailed in Section 3. Cylindrical and shellular rotation profiles are examined in Sections 4.2.1 and 4.2.2, respectively. A qualitative analysis of the occurrence of modes with quasi-periodic orbits of characteristics follows in Section 4.2.3.

4.2.1. Cylindrical rotation

We describe in this paragraph three representative $m = 0$ eigenmodes obtained with our cylindrical rotation profile: a D mode (the hyperbolic domain covers the whole shell), and two DT modes (the hyperbolic domain covers a fraction of the shell). All three calculations have a spectral resolution $N_r = 450 \times L = 800$.

Fig. 6 displays the results for a D mode with eigenfrequency $\Omega_p \approx 0.91\Omega_{\text{ref}}$, obtained for $\varepsilon = -0.3$ (recall that for cylindrical rotation, Ω_{ref} denotes the shell's angular frequency at the rotation axis). The top-left panel depicts contours of the mode's kinetic energy in a meridional quarter-plane[†]. Results are shown only for positive values of z , for reasons of symmetry exposed in Section 3.1. This D mode essentially features a shear layer following a short-period wave attractor, which is overplotted by a thick white curve. The mode's kinetic energy is maximum near the rotation axis, like in the case of solid-body rotation (Rieutord & Valdettaro 1997). Note also the presence of another shear layer tangent to the shell's inner core. As already highlighted in Section 3.1, rays in a meridional plane are curved by differential rotation. This is also illustrated in the top-right panel of Fig. 6, which displays the paths of characteristics obtained by solving Eq. (3.8), given a particular initial location (here at $s = 0$ and $z = 0.75R$). The patterns of the viscous shear layer (left panel) and of the paths of characteristics under the short-wavelength approximation (right panel), are in excellent agreement. Paths of characteristics focus towards the aforementioned wave attractor, depicted by a red curve in this panel. Upon varying initial conditions, we have checked that this is the only attractor in the shell for this particular eigenfrequency. The bottom panel of Fig. 6 shows the good convergence in spectral resolution for this mode.

We present in Fig. 7 the results for an $m = 0$ DT mode with $\Omega_p \approx 1.33\Omega_{\text{ref}}$ and $\varepsilon = -0.4$. The left panel shows a meridional cut of the kinetic energy for this mode, which exhibits again a shear layer following an attractor of characteristics. The mode's pattern features reflexions on the inner and outer edges of the shell, as well as on a turning surface located at $s \sim 0.75R$. The radius at which the shear layer bounces off is in good

[†] In all our contour plots, the simulation parameters are summarized below the x-axis (spectral resolution $N_r \times L$, azimuthal wavenumber m , Ekman number E , shell's aspect ratio η , differential rotation rate ε or σ for cylindrical or shellular rotation profiles, respectively). Similarly, the complex eigenfrequency is indicated in the bottom-left corner of the shell: the absolute value of its real part is denoted by $|\omega|$ (in units of Ω_{ref}), and its imaginary part by τ (in units of Ω_{ref}^{-1} ; negative values of τ correspond to damped modes).

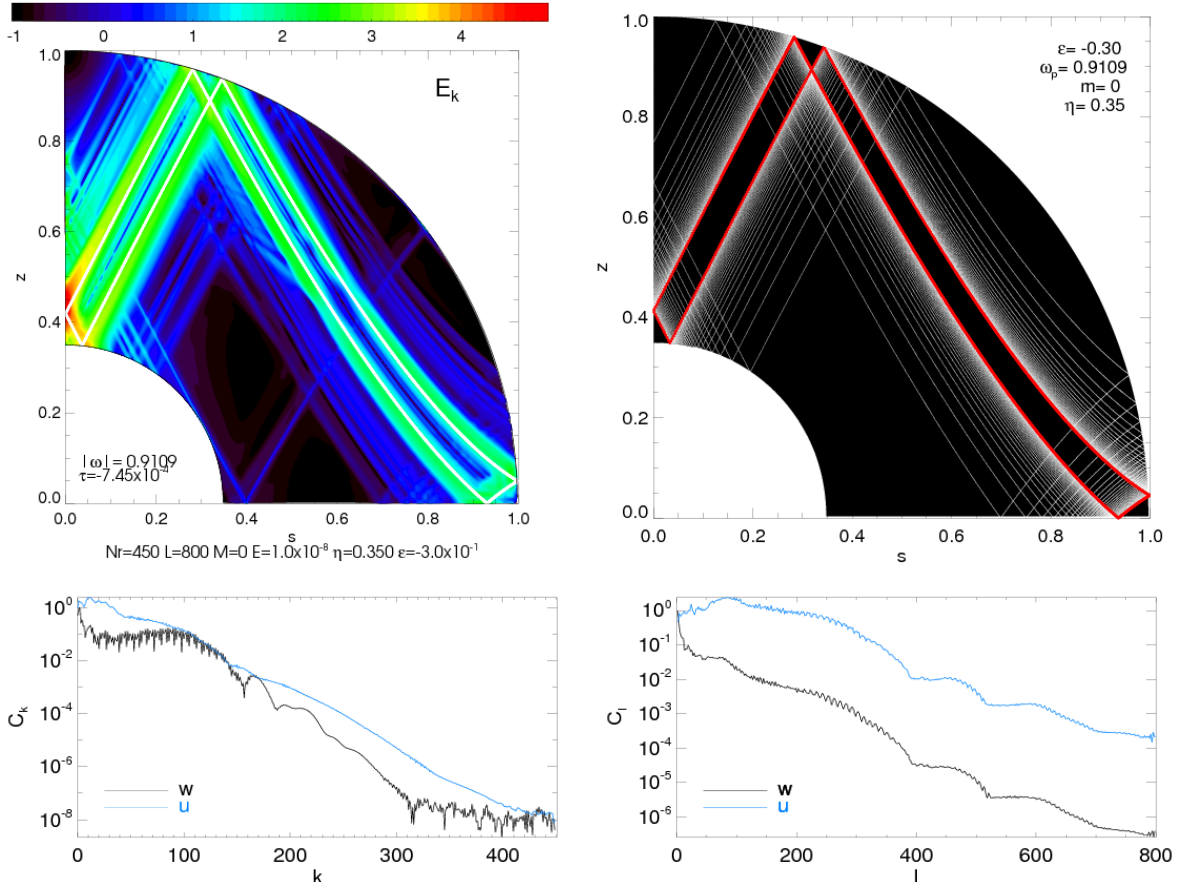


FIGURE 6. Top left: meridional cut of the kinetic energy for a D mode with eigenfrequency $\Omega_p \approx 0.91\Omega_{\text{ref}}$, obtained with $E = 10^{-8}$ and cylindrical rotation profile $\Omega(s)/\Omega_{\text{ref}} = 1 - 0.3(s/R)^2$. An attractor of characteristics is overplotted by a solid white curve. Top right: a few paths of characteristics are shown to converge towards the aforementioned attractor, which is displayed here by a red curve. Bottom: spectral content of the radial (u) and orthoradial (w) components of the velocity field for this mode. Chebyshev and spherical harmonic coefficients are shown in the left and right panels, respectively.

agreement with the (numerical) solution to $\xi(s) = 0$, shown by a dashed line. A few paths of characteristics, obtained again by solving Eq. (3.8), are shown by white curves in the right panel of Fig. 7, which rapidly converge toward the above attractor (in red in this panel). We point out that there exists another attractor for this eigenfrequency and this differential rotation rate, which is overplotted by a blue curve.

An interesting DT mode is finally illustrated in Fig. 8 for $\Omega_p \approx 1.10\Omega_{\text{ref}}$ and $\varepsilon = -0.4$, where a shear layer follows an attractor for an arbitrarily small inner core. In this particular calculation, $\eta = 0.05$. This example highlights that, in contrast to solid-body rotation, attractors may be formed by reflexions on one of the shell's edges (the surface in this case) and a turning surface. This property is also shared by gravito-inertial modes in stably-stratified rotating fluids (Friedlander 1982; Dintrans *et al.* 1999). The mode shown in Fig. 8 indicates that, with cylindrical rotation, wave attractors may exist independently of a putative inner core inside the shell. We show below that the same is true with shellular rotation.

4.2.2. Shellular rotation

We describe in this paragraph a few axisymmetric ($m = 0$) eigenmodes obtained with our shellular rotation profile, $\Omega(r)/\Omega_{\text{ref}} = (r/R)^\sigma$ (here, Ω_{ref} denotes the angular frequency at the shell's surface). An overview of the impact of shellular rotation is illustrated in Fig. 9 for a singular mode with eigenfrequency $\Omega_p \approx 1.11\Omega_{\text{ref}}$ for solid-body rotation. Contours of the kinetic energy in a meridional quarter-plane are shown for σ equal to 0 (top-left panel),

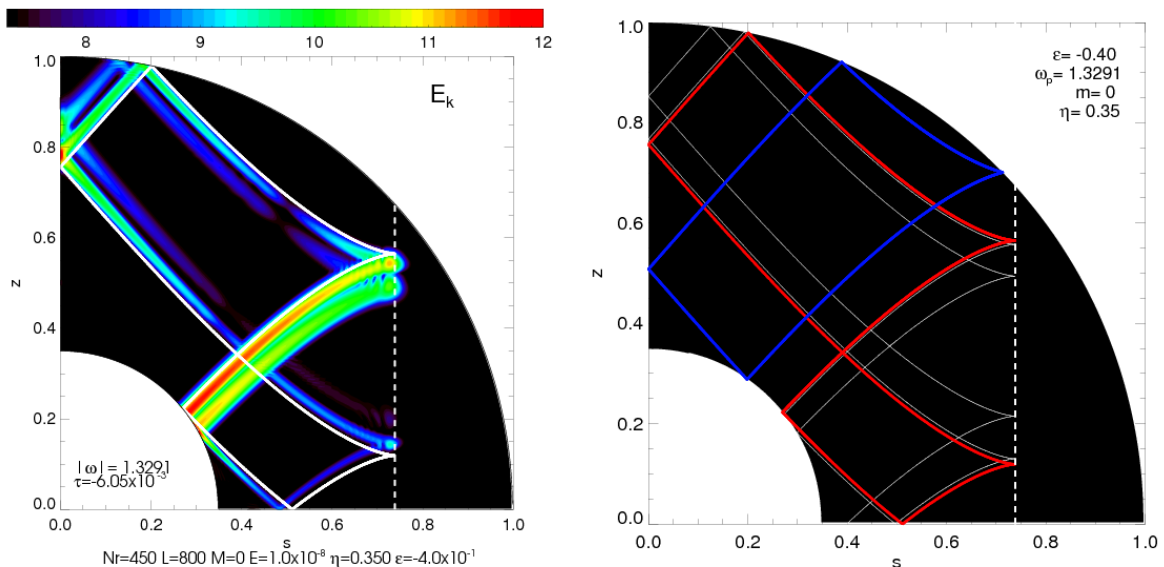


FIGURE 7. Left: meridional slice of the kinetic energy for a DT mode with $\Omega_p \approx 1.33\Omega_{\text{ref}}$, $E = 10^{-8}$, and $\epsilon = -0.4$. The shear layer follows a wave attractor (solid curve). The dashed line shows the location of the turning surface inferred from Eq. (3.9). Right: a few paths of characteristics are depicted by white curves, which converge toward the aforementioned wave attractor (red curve). A second wave attractor is shown in blue.

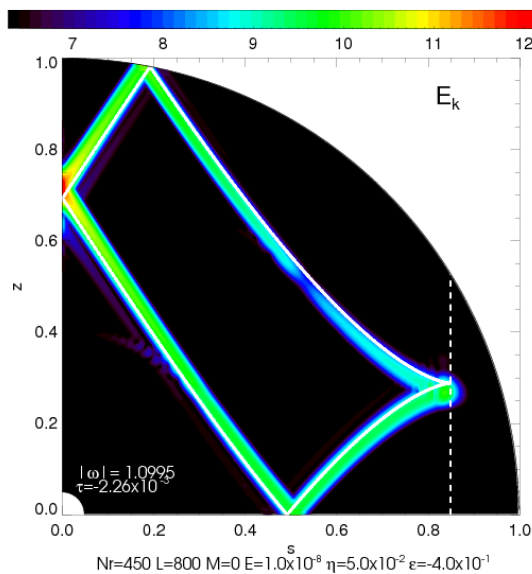


FIGURE 8. Meridional slice of the kinetic energy for a DT mode with $\Omega_p \approx 1.10\Omega_{\text{ref}}$, $E = 10^{-8}$, $\eta = 0.05$ and $\epsilon = -0.4$. The turning surface is shown by a dashed line. For an arbitrarily small inner core, the shear layer follows an attractor of characteristics, shown by the solid curve.

-0.5 (top-right), and -1.3 (bottom-left). Calculations were carried out as a sequence, the eigenfrequency of the least-damped mode obtained with differential rotation rate σ being used as the guess frequency for the next run with differential rotation rate $\sigma - d\sigma$. In this series of runs, $d\sigma = 0.01$, $E = 10^{-7}$, and the spectral resolution is $N_r = 250 \times L = 600$. The contour panels in Fig. 9 show how the shape of the shear layer, and thus that of the wave attractor it focuses on (which curve), is progressively deformed by shellular rotation. Note the presence of a turning surface for $\sigma = -1.3$ (dashed curve). Not surprisingly, the mode's eigenfrequency increases with increasing the steepness σ of the rotation profile. We also observe that the mode's damping rate decreases in absolute value for steeper

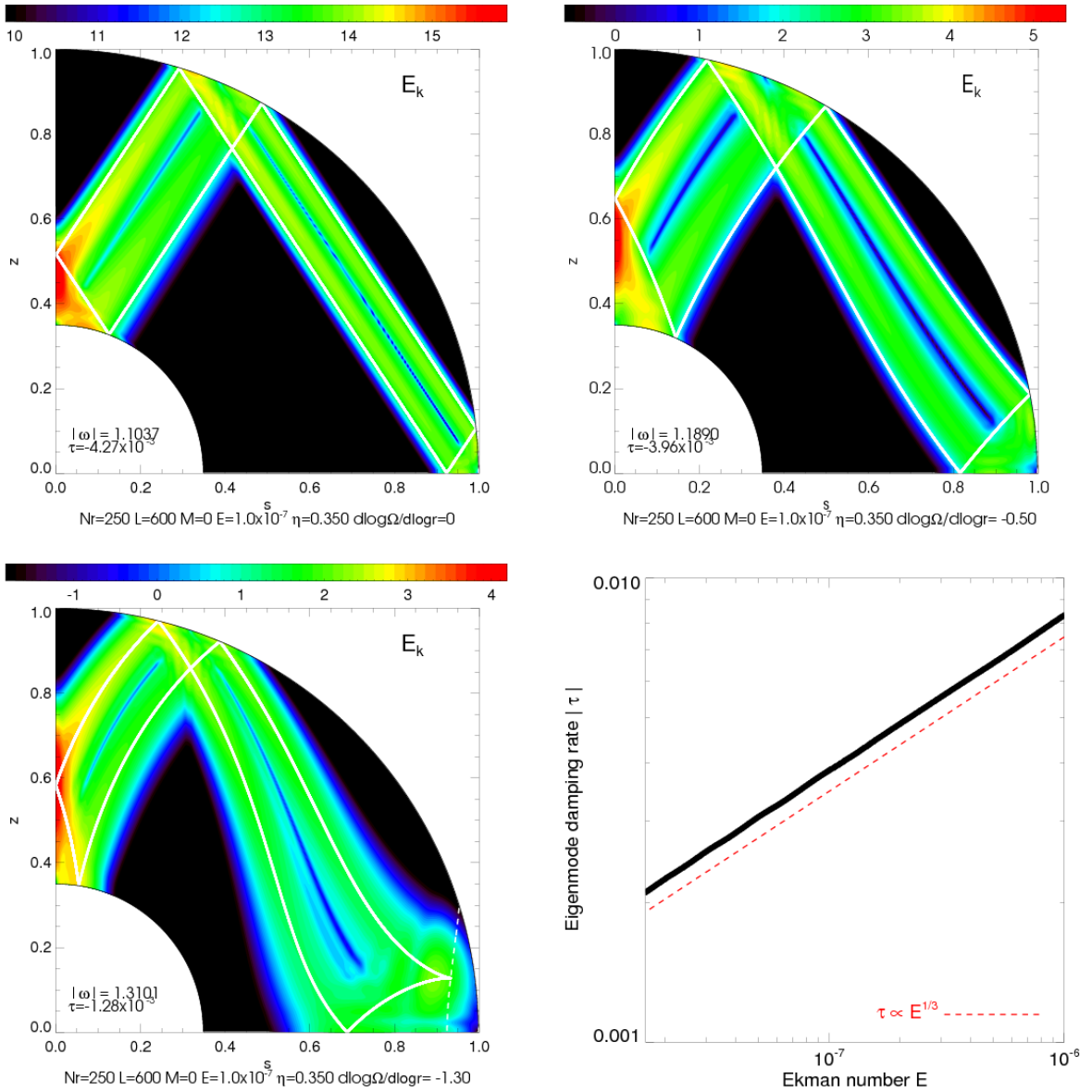


FIGURE 9. Meridional cuts of kinetic energy for a given eigenmode with $E = 10^{-7}$ and $\sigma = 0$ (top-left), -0.5 (top-right), and -1.3 (bottom-left). The shear layer for this mode follows an attractor overplotted by a solid curve in each of these panels. The dashed curve in the bottom-left panel displays the location of a turning surface, given by Eq. (3.21). The bottom-right panel shows that the damping rate of previous mode with $\sigma = -1$ scales as $E^{1/3}$, with E the Ekman number.

rotation profiles. Some insight into the asymptotic behavior of this mode at small Ekman numbers is given by the bottom-right panel in Fig. 9. The damping rate of the mode with $\sigma = -1$ is displayed for Ekman numbers varying from 10^{-6} down to about 2×10^{-8} . Runs were also performed as a series, the eigenfrequency of the least-damped mode obtained at Ekman number E being used as the guess frequency for the run with Ekman number $E - dE$ (the spectral resolution is progressively increased with decreasing E). The dashed line shows that the damping rate of this particular mode scales proportional to $E^{1/3}$, a scaling that is reminiscent of the solid-body rotation case (Rieutord & Valdettaro 1997).

The aforementioned $E^{1/3}$ scaling of the mode's damping rate is not the only possible scaling for shellular rotation in the limit of vanishing viscosities. This is illustrated in the top-left panel of Fig. 10 for a particular DT mode having a turning surface that encom-

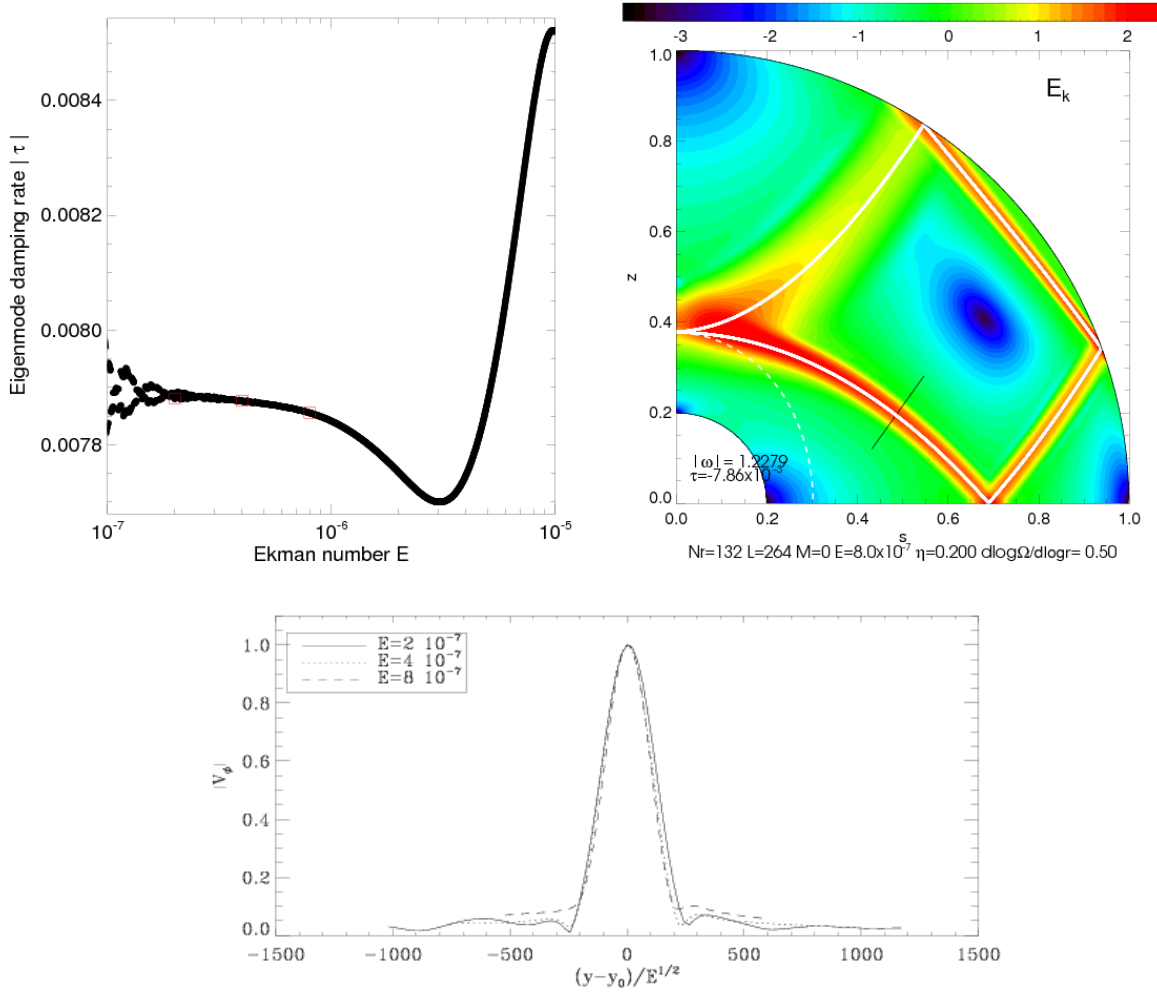


FIGURE 10. Top-left: evolution of the damping rate ($|\tau|$) with decreasing Ekman number for a DT eigenmode with shellular rotation, $\Omega(r) \propto r^{0.5}$, $\eta = 0.2$, which features a detached shear layer tangent to a turning surface at the location of the rotation axis. Top-right: contours of kinetic energy for the mode depicted by the rightmost open square in the top-left panel ($E \approx 8.0 \times 10^{-7}$). The thick white curve shows the attractor of characteristics followed by the shear layer, and the dashed curve the location of a turning surface that encompasses the inner core. Bottom: cut of the perturbed velocity across the shear layer (at the location depicted by a black line in the top-right panel) for the three modes displayed with open square symbols in the top-left panel.

passes the inner core, and for which the damping rate is found to be roughly independent of E . This property is reminiscent of quasi-modes associated with critical layers (see, e.g., Le Dizès 2004). However, the physical mechanism leading to such a damping rate must be different because the DT mode we consider is axisymmetric, so that no corotation singularity exists. Contours of kinetic energy for this new type of quasi-modes are shown in the top-right panel of Fig. 10, where we see that the mode is dominated by a shear layer following a wave attractor tangent to the turning surface at the location of the rotation axis (note that, since the turning surface encompasses the inner core at $r = 0.35R$, this mode exists for arbitrarily small inner cores, akin to the mode shown in Fig. 8 for cylindrical calculation). We have carried out additional calculations with a slightly different eigenfrequency at given Ekman number, such that the wave attractor no longer hits the tangent critical point at the rotation axis. We found that the damping rate is no longer independent of E for the same range of Ekman numbers as in the top-left panel of Fig. 10. It suggests that the tangent critical point plays a prominent role in getting a damping rate independent of E . Such scaling demands a very thin detached shear layer, namely $\mathcal{O}(E^{1/2})$ -wide. This is indeed confirmed by the velocity profiles depicted in the bottom

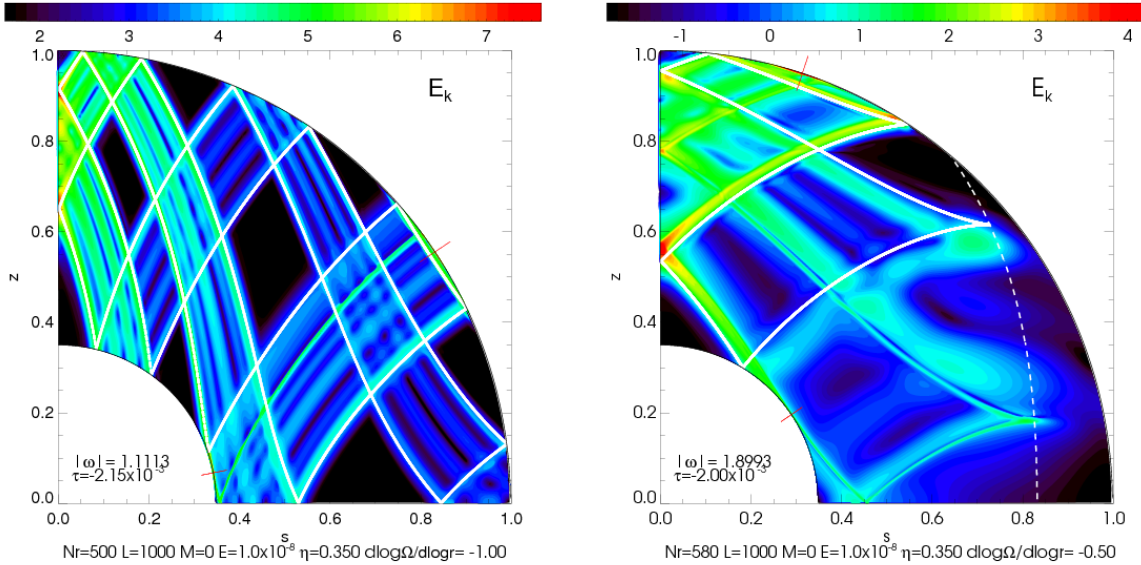


FIGURE 11. Kinetic energy of two axisymmetric D and DT eigenmodes with shellular rotation, for $E = 10^{-8}$. Left: D mode with $\Omega_p \approx 1.11\Omega_{\text{ref}}$ and $\Omega(r) \propto r^{-1}$. Right: DT mode with $\Omega_p \approx 1.90\Omega_{\text{ref}}$ and $\Omega(r) \propto r^{-0.5}$. Red ticks show the values of the inner and outer critical latitudes given by Eqs. (3.28) and (3.29).

panel of Fig. 10 at three Ekman numbers (shown by red squares in the top-left panel of Fig. 10). Of course, this numerical result does not prove that this vigorously damped mode survives at vanishingly small viscosities, and that it is thus a new type of quasi-modes. Still, it calls for a detailed analysis of this new type of detached shear layers, which are as thin as Ekman boundary layers.

We now present the results of simulations for two D and DT eigenmodes at smaller Ekman number ($E = 10^{-8}$) and higher spectral resolution ($N_r = 500$ or $N_r = 580$, $L = 1000$). Results are shown in Fig. 11. A D mode with $\Omega_p \approx 1.11\Omega_{\text{ref}}$ and $\Omega \propto r^{-1}$ is shown in the left panel of this figure. A shear layer is clearly visible that follows an attractor of characteristics, calculated through Eq. (3.18) and overplotted by a white curve. We note again the excellent agreement between the overall pattern of the viscous shear layer, and the paths of characteristics. Because of its finite width, the shear layer also excites the critical latitude singularity, on both the inner and outer edges of the shell. The location of the inner and outer critical latitudes, given by Eqs. (3.28) and (3.29), is depicted by red ticks, and it is clear that the shear layer is tangent to the inner and outer edges of the shell at these latitudes. Lastly, the right panel of Fig. 11 shows a DT mode with $\Omega_p \approx 1.90\Omega_{\text{ref}}$ and $\Omega \propto r^{-0.5}$. In this case again, the mode's pattern suggests that part of the shear layer approximately follows a wave attractor, shown by a white curve, and that part of it is tangent to both the inner and outer edges of the shell at the critical latitudes.

4.2.3. Quasi-periodic orbits of characteristics

The results presented in the previous paragraphs all feature modes that are associated with short-period attractors. These modes are all singular at vanishing viscosity. One may however wonder about the existence of regular modes, which exist in the inviscid case, or at least modes that display shear layers only at unphysically small viscosities. Such modes are necessarily associated with weak attractors or with quasi-periodic orbits of characteristics. To assess the occurrence of such orbits of characteristics, we have evaluated the Lyapunov exponent of various pairs of characteristics. The Lyapunov exponent measures the rate of convergence of two close characteristics after multiple reflections on the inner and outer edges of the shell, and on turning surfaces when present. For solid-body rotation, the latitudes of two successive reflections on the inner or outer edges can be related analytically, and the Lyapunov exponent can therefore be determined semi-analytically

(Rieutord *et al.* 2001). This is no longer the case with differential rotation: Lyapunov exponents must be evaluated numerically by integrating paths of characteristics given some initial conditions.

For the symmetry reasons underlined in Sect. 3, paths of characteristics are calculated in a meridional quarter-plane with reflections on to the rotation axis ($s = 0$) and the equatorial axis ($z = 0$). Because turning surfaces may prevent reflections on either axis, we define the two following Lyapunov exponents associated with reflections on the equatorial axis (denoted by Λ_s) and on the rotation axis (Λ_z):

$$\Lambda_s = \lim_{N_s \rightarrow \infty} \frac{1}{N_s} \sum_{k=1}^{N_s} \ln \left| \frac{ds_{k+1}}{ds_k} \right| \quad \text{and} \quad \Lambda_z = \lim_{N_z \rightarrow \infty} \frac{1}{N_z} \sum_{k=1}^{N_z} \ln \left| \frac{dz_{k+1}}{dz_k} \right|, \quad (4.5)$$

where ds_k and dz_k are the separation between two characteristics after k reflections on the equatorial and rotation axes, respectively.

A negative Lyapunov exponent means that the two characteristics get progressively closer to each other, converging towards an attractor. The more negative this value, the faster the convergence (and the stronger the attractor). In contrast, small-amplitude Lyapunov exponents may correspond to quasi-periodic orbits of characteristics. Because two attractors may co-exist in the shell at a given eigenfrequency, and for averaging purposes, we have considered five pairs of initial conditions and four regions of the shell located near the rotation or equatorial axes, and near the shell's surface or the inner core (that is, twenty pairs of characteristics). The most negative value amongst the (averaged) Lyapunov exponents obtained in the above four regions defines what we now refer to *the* Lyapunov exponent, and which we denote by Λ . If two attractors co-exist in the shell, our method will thus retain the one with the shortest period.

Lyapunov exponents obtained for $m = 0$ and a few rotation profiles are displayed in the top panel of Fig. 12. The range of eigenfrequencies $[0.2\Omega_{\text{ref}}, 2\Omega_{\text{ref}}]$ is sampled with 1800 values (Ω_{ref} is the angular frequency at the shell's surface). The case with solid-body rotation and $\eta = 0.35$ is depicted by a red curve. It can be compared with the semi-analytic results of Rieutord *et al.* (2001), see the left panel of their figure 6 (where $\Omega_p/2\Omega_{\text{ref}}$ is displayed in x-axis). This comparison shows that our numerical method reproduces qualitatively well the ranges of frequencies at which strong attractors and quasi-periodic orbits of characteristics exist. Quantitative differences inevitably exist, however, and are most significant for attractors with moderate Lyapunov exponents (that is, Λ in the range $[-0.5, -0.2]$), which our method tends to underestimate.

Results obtained with shellular rotation and $\sigma = 0.5$ are overplotted by a black curve in the top panel of Fig. 12. For this rotation profile, inertial modes exist for eigenfrequencies $|\Omega_p| \lesssim 2.2\Omega_{\text{ref}}$ (see, e.g., Fig. 3) and the transition from D to DT modes occurs at $|\Omega_p| \approx 1.18\Omega_{\text{ref}}$ (see Eq. 3.25). For $\Omega_p \leq 1.18\Omega_{\text{ref}}$ (D modes only), the shellular case features the same attractors as in the case with solid-body rotation. However, attractors are shifted toward lower frequencies with shellular rotation as the shell's interior rotates at a slower pace in this case. Lyapunov exponents also take very similar values since shellular rotation changes the overall shape of these attractors without altering their period. For $\Omega_p \geq 1.18\Omega_{\text{ref}}$, the shellular case displays many more attractors, which form through reflections on to turning surfaces that encompass the inner core. Finally, results obtained with the same shellular profile, but for the full sphere ($\eta = 0$) are also shown by the blue curve. The full sphere only supports DT modes in this case. For $\Omega_p \gtrsim 1.4\Omega_{\text{ref}}$, results are identical to those obtained with $\eta = 0.35$, as in both cases the turning surface occupies radii $r > 0.35R$. Differences for $\Omega_p \lesssim 1.4\Omega_{\text{ref}}$ are essentially through the strong attractor at $\Omega_p \sim 0.8\Omega_{\text{ref}}$, which is related to a turning surface located at $r < 0.35R$.

Although the above results have been obtained with a fixed profile of shellular rotation, the general conclusion that can be drawn is that, just like for solid-body rotation, a differentially rotating spherical shell may harbour both short-period attractors and quasi-periodic orbits of characteristics. Their occurrence depends on the rotation profile and the sphere's aspect ratio. An example of $m = 0$ D mode with a weak attractor, obtained

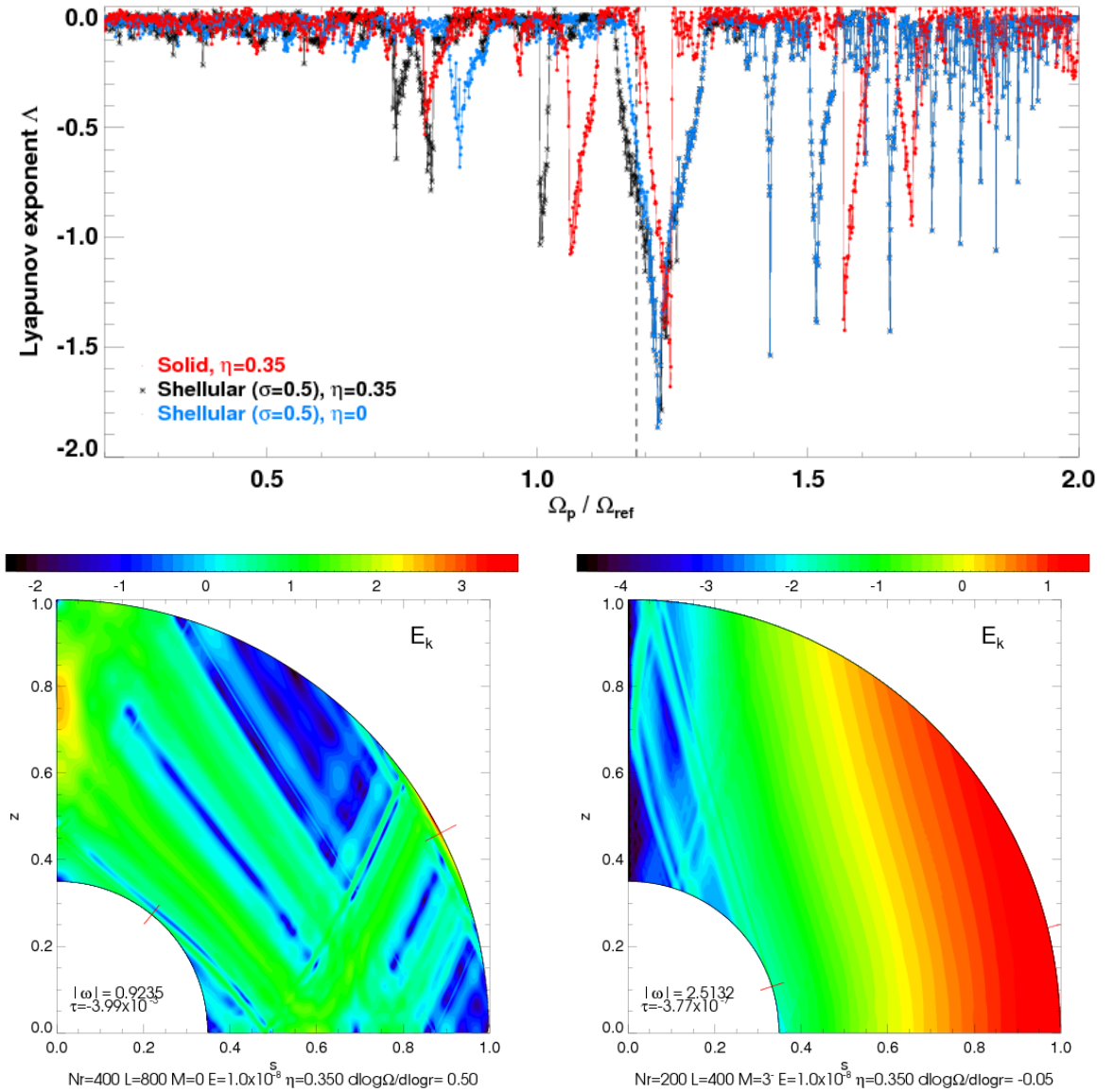


FIGURE 12. Top: Lyapunov exponent obtained for $\eta = 0.35$ and $m = 0$. Results with solid-body rotation (red curve) are compared to shellular rotation with $\sigma = 0.5$ (black curve). The vertical dashed line displays the eigenfrequency that separates D and DT modes for this rotation profile. Results with shellular rotation, $\sigma = 0.5$ and for a full sphere ($\eta = 0$) are overplotted in blue. Bottom left: meridional cut of the kinetic energy for an $m = 0$ D mode with $\sigma = 0.5$ and $\Omega_p \approx 0.92\Omega_{\text{ref}}$, which features a weak attractor (the Lyapunov coefficient is a few percent). Bottom-right: meridional cut of the kinetic energy for an $m = 3$ D mode with $\Omega_p \approx -2.5\Omega_{\text{ref}}$ and $\sigma = -0.05$. This mode has been obtained assuming asymmetry with respect to the equatorial plane.

for $E = 10^{-8}$, $\sigma = 0.5$ and $\eta = 0.35$, is shown in the bottom-left panel of Fig. 12, and it is clear that the kinetic energy for this mode is more homogeneously distributed than in the modes illustrated in previous figures.

While the calculation of Lyapunov coefficients unambiguously shows the existence of quasi-periodic orbits of characteristics, it is difficult to use it to prove or disprove the existence of regular modes for which Λ should strictly vanish (Dintrans *et al.* 1999; Rieutord *et al.* 2001). We have looked for regular modes with differential rotation, though. It was suggested by Rieutord *et al.* (2001) that toroidal modes, with Doppler-shifted eigenfrequencies of the form $\tilde{\Omega}_p = 2\Omega/(m+1)$ (m is the azimuthal wavenumber) are the only regular modes in a rigidly-rotating spherical shell. We have followed the toroidal mode

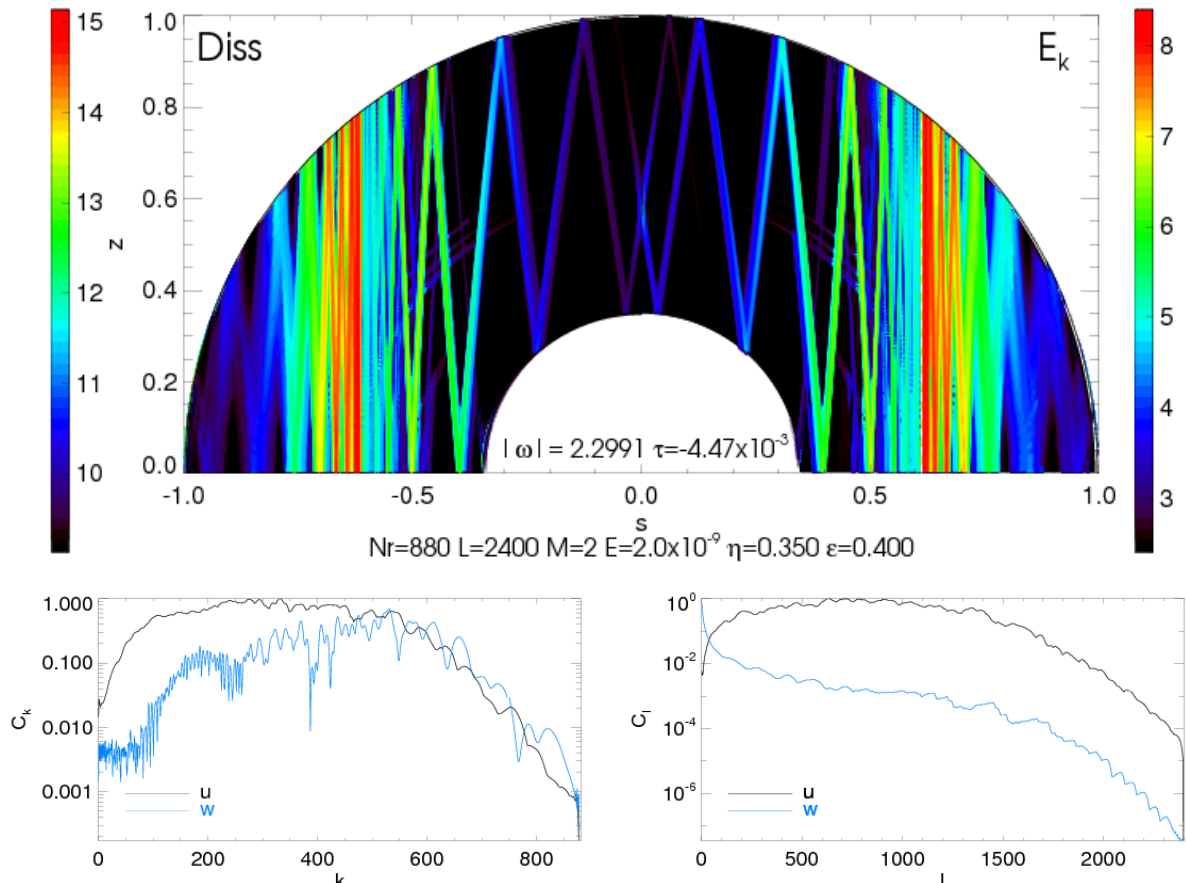


FIGURE 13. Top: meridional cut of the viscous dissipation (left quadrant) and kinetic energy (right quadrant) for a D mode with $m = 2$, eigenfrequency $\Omega_p \approx -2.3\Omega_{\text{ref}}$, $E = 2 \times 10^{-9}$ and cylindrical rotation profile $\Omega(s) = 1 + 0.4s^2$. A corotation resonance (critical cylinder) is located at $s \approx 0.6$. Bottom: spectral content of the radial (u) and orthoradial (w) components of the velocity field for this mode. Chebyshev and spherical harmonic coefficients are shown in the left and right panels, respectively.

with $m = 3$ by slowly increasing the differential rotation rate (for shellular rotation). As shown in the bottom-right panel of Fig. 12, even for values of σ as small as a few percent, the mode's regularity fades away. Although most of the kinetic energy remains contained in a smooth structure reminiscent to that of the toroidal mode, ray structures develop, in particular from the inner critical latitude. Therefore, inertial oscillations with differential rotation seem to be all singular in the limit of vanishing Ekman numbers. A similar result was obtained for gravito-inertial modes (Friedlander 1982; Dintrans *et al.* 1999), which also satisfy a PDE of mixed type, analogous to Eq. (3.1).

4.3. Non-axisymmetric eigenmodes: corotation resonances

We briefly examine in this section the behavior of viscous, non-axisymmetric inertial waves when their frequency in the rotating frame ($\tilde{\Omega}_p$) vanishes inside the shell. Such corotation resonances will be referred to as critical cylinders for cylindrical rotation, and as critical layers for shellular rotation. We present results of linear numerical calculations, which we compare to the analysis of Section 3. Cylindrical and shellular rotation profiles are considered in Sections 4.3.1 and 4.3.2, respectively.

4.3.1. Cylindrical rotation

An example of $m = 2$ D eigenmode with a critical cylinder is displayed in Fig. 13. This mode is obtained for $\varepsilon = 0.4$, $E = 2 \times 10^{-9}$, and the very high spectral resolution $N_r = 880 \times L = 2400$. Its eigenfrequency $\Omega_p \approx -2.3\Omega_{\text{ref}}$ (a negative Ω_p is required for

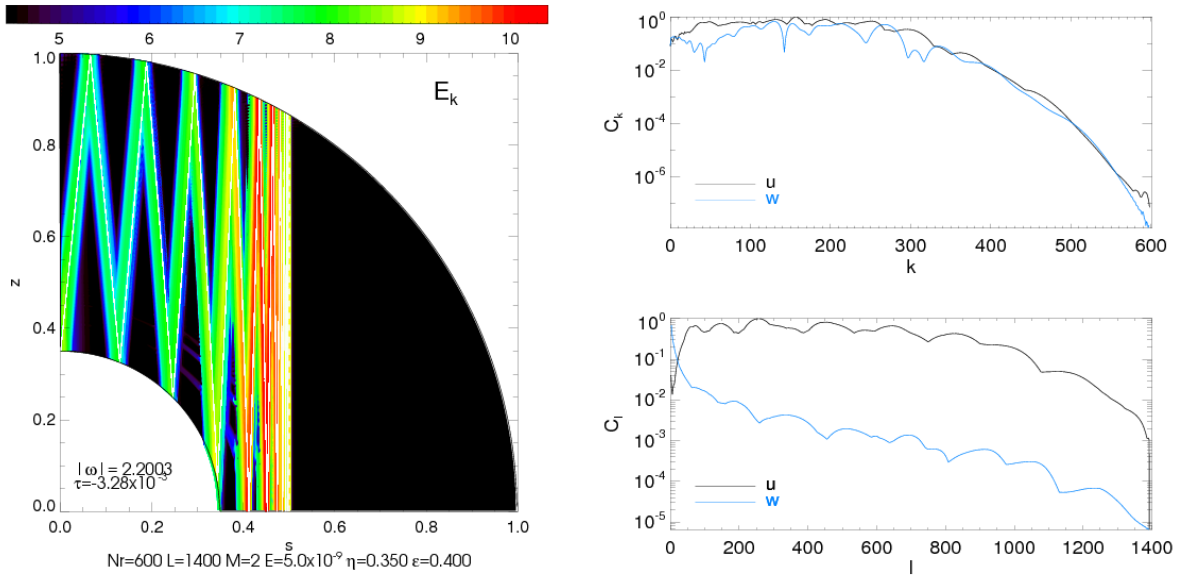


FIGURE 14. Left: meridional cut of the kinetic energy for a D mode with $m = 2$, eigenfrequency $\Omega_p \approx -2.20\Omega_{\text{ref}}$, $E = 5 \times 10^{-9}$, and $\varepsilon = 0.4$. A corotation resonance is located at $s \approx 0.5$. A few paths of characteristics are overplotted by white curves. Right: spectral content of the radial (u) and orthoradial (w) components of the velocity field for this mode. Chebyshev and spherical harmonic coefficients are shown in the top and bottom sub-panels, respectively.

an $m > 0$ eigenmode to have a corotation resonance within the shell). The top panel of Fig. 13 shows a meridional cut of the viscous dissipation (left quadrant) and of the kinetic energy (right quadrant) for this mode. The mode's spectral content is also displayed in the bottom panel of Fig. 13 to highlight the good convergence in spectral resolution obtained for this mode. According to Eq. (3.13), a critical cylinder is located at $s_{\text{crit}} \approx 0.61R$. Near this location, the mode's kinetic energy and viscous dissipation are discontinuous. Upon approaching corotation from $s > s_{\text{crit}}$, the mode's pattern in a meridional quarter-plane becomes more and more parallel to the rotation axis, and according to Eq. (3.16), the component of the group velocity perpendicular to the critical cylinder should eventually cancel out at corotation, formally preventing the mode from crossing the critical cylinder. Our simulation indicates that, in a moderately viscous fluid, waves get dramatically absorbed upon crossing corotation, but keep on propagating at $s < s_{\text{crit}}$ with a much reduced amplitude.

We point out that the fraction of the mode's amplitude that is effectively transmitted across corotation depends on the mode of interest. A similar $m = 2$ mode with eigenfrequency and Ekman number slightly increased to $\Omega_p \approx -2.20\Omega_{\text{ref}}$ and $E = 5 \times 10^{-9}$, respectively, shows no significant transmission in Fig. 14, as if the incoming wave was fully absorbed at corotation. The contour plot in the left panel of this figure gives an upper limit for the kinetic energy transmission factor $\sim 10^{-6}$. Note that in the example shown in Fig. 14, linear inertial waves propagate from the inside outwards, whereas Fig. 13 shows an opposite direction of propagation (from the outside inwards). It is likely due to a mode selection, with different modes existing on each side of the corotation radius.

4.3.2. Shellular rotation

An example of $m = -6$ eigenmode with a critical layer is depicted in Fig. 15. For this mode, $E = 6 \times 10^{-9}$, $\Omega(r) \propto r^{-0.2}$, and the spectral resolution is $N_r = 500 \times L = 1401$. This mode's eigenfrequency $\Omega_p \approx 7.11\Omega_{\text{ref}}$ (this time, a positive Ω_p is required for an $m < 0$ eigenmode to have a corotation resonance within the shell). Contours of the kinetic energy in a meridional quarter-plane are shown together with the mode's spectral content. The critical layer is depicted by a white solid curve in the left panel, and we see that, in contrast to cylindrical rotation, waves cross the critical layer without experiencing

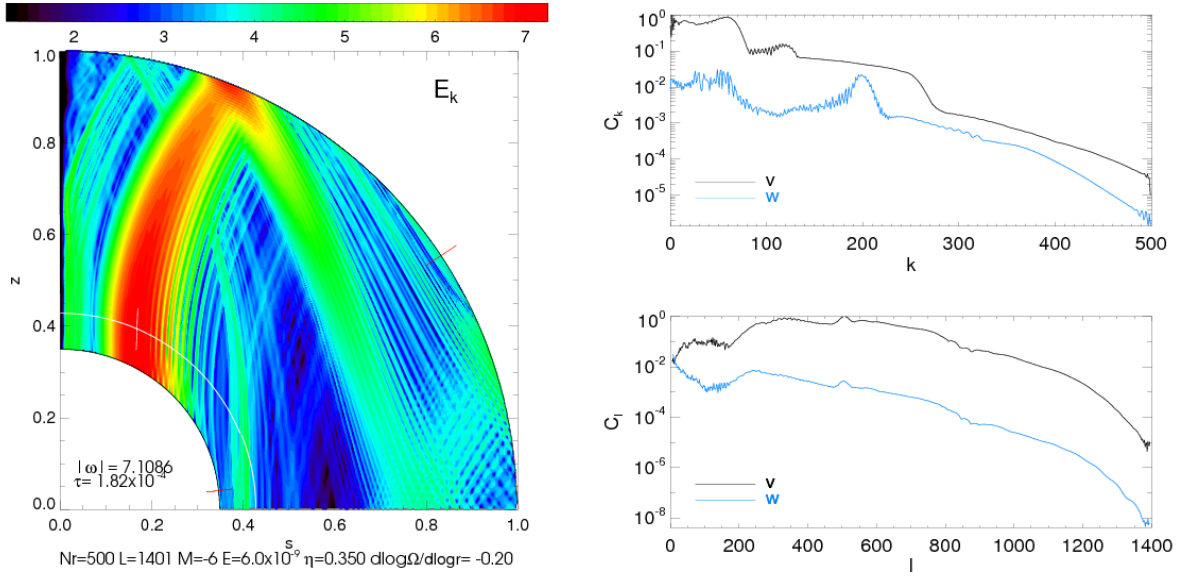


FIGURE 15. Left: meridional cut of the kinetic energy for a growing eigenmode with $E = 6 \times 10^{-9}$, $\sigma = -0.2$, $\Omega_p \approx 7.11\Omega_{\text{ref}}$ and $m = -6$. The location of the critical layer is depicted by a solid curve, along which a white tick shows the local slope of characteristics given by Eq. (3.34). Red ticks show the inner and outer critical latitudes. Right: spectral content of the radial (the quantity $v = xu$ is displayed here) and orthoradial (w) components of the velocity field for this mode. Chebyshev and spherical harmonic coefficients are in the top and bottom sub-panels, respectively.

significant absorption. The local analysis carried out for the inviscid case in Section 3.2.3 shows that (linear) inertial waves may indeed cross a critical layer with a (formally) divergent group velocity at the critical layer. This occurs if $|k_z| \rightarrow 0$ (paths of characteristic then being locally parallel to the rotation axis), or if $\mathcal{B} \rightarrow 0$ (paths of characteristics having a finite slope at the critical layer). The white tick displayed on top of the critical layer in the left panel of Fig. 15 shows the local slope of characteristics if $\mathcal{B} = 0$, which is given by Eq. (3.34). The large slope obtained in this case (due to the small value of $|\sigma|$) prevents a clear distinction with the case $|k_z| \rightarrow 0$. The local analysis also shows the possibility that the group velocity formally vanishes at a critical layer (when $|k_s| \rightarrow \infty$ locally), much like in the case of cylindrical rotation. However, we have not found such situation in our numerical exploration of modes featuring a critical layer.

The most salient feature of the mode shown in Fig. 15 is that it is found to be unstable: its growth rate, τ , is positive. We have examined in some more details this particular mode by varying the Ekman number, keeping the same spectral resolution. We have varied E in the range $[4 \times 10^{-9} - 3.2 \times 10^{-8}]$. Results are shown in Fig. 16, where the mode's growth rate is depicted as a function of the Ekman number. There is a transition occurring near $E_c \approx 10^{-8}$: $\tau < 0$ (the mode is decaying) for $E > E_c$, whereas $\tau > 0$ (the mode is growing) for $E < E_c$. The mode's growth rate is actually well approximated by a linear function of E near this transition: $\tau = \alpha(E - E_c)$, with $\alpha < 0$. Although not displayed here, the kinetic energy obtained in the simulations with $E \gtrsim 10^{-8}$ is very similar to that of the left panel in Fig. 15, except for the thick shear layer on each side of corotation, which is found to progressively disappear with increasing E . The very good convergence in spectral resolution obtained in these calculations (as is highlighted by the right panels in Fig. 15), and the fact we have been able to successfully follow this particular mode with decreasing Ekman number (see Fig. 16) makes us confident that the positive growth rate that we obtain at small Ekman numbers is physical, and not a numerical artifact arising from truncature or round-off errors. It is tempting to interpret this result based on the local dispersion relation obtained at Eq. (3.30). It is possible indeed that the instability we have obtained in our simulations is related to the Goldreich-Schubert-Fricke instability

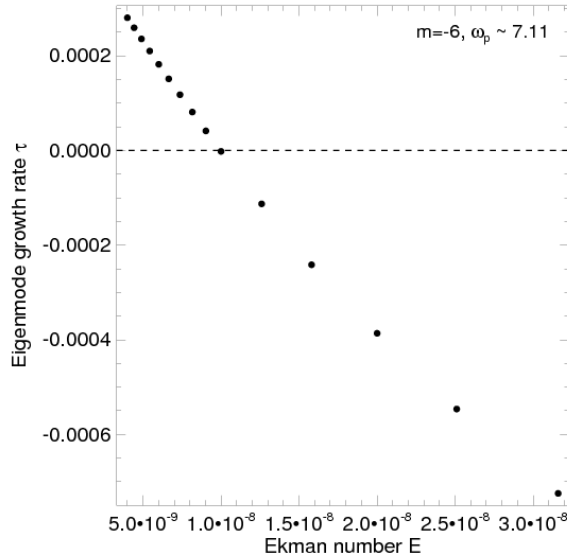


FIGURE 16. Growth rate for the same eigenmode as in Fig. 15 ($m = -6$, $\sigma = -0.2$, $\Omega_p \approx 7.11\Omega_{\text{ref}}$) with varying the Ekman number E . The mode becomes unstable for $E \lesssim 10^{-8}$.

in the limit of an incompressible inviscid fluid. The physical mechanism that drives the instability in our model requires a specific investigation that is postponed for future work.

5. Astrophysical implications and concluding remarks

The late evolution of the orbital elements and spin of short-period extrasolar planets, or of close binary-star systems, is primarily driven by tidal interactions. The tidal torque acting on a gravitationally perturbed body encompasses the equilibrium torque, which arises from the quasi-hydrostatic tidal bulge setting around the body, and the dynamical torque, due to tidally forced internal waves propagating inside the body. Inertial waves may propagate in convective regions of stars and planets, where the Coriolis force is the main restoring force. Gravito-inertial waves may propagate in radiative zones, where buoyancy and rotation act as restoring forces. The magnitude of the dynamical torque is directly related to how much angular momentum is deposited by internal waves, which has a complex dependency upon the forcing potential (amplitude and frequency), and the body's internal properties (see, e.g., Ogilvie & Lin 2004, 2007; Ogilvie 2009; Rieutord & Valdettaro 2010). In many dynamical studies of short-period exoplanets, the tidal torque of the central star is parametrized by a single, dimensionless tidal quality factor Q , which should be thought of, and determined as, a frequency-averaged quantity (Ogilvie 2009).

Prior to an investigation of tidally-forced inertial waves in differentially rotating stars and planets, we have examined the propagation properties of linear inertial waves in a rotating fluid body contained in a spherical shell, taking into account the effects of differential rotation. We have used a simple model that consists of an incompressible homogeneous fluid, with dissipation occurring through viscous forces. This fluid model is an intentionally simplified model for the convective zones of stars and planets. We have considered two particular rotation profiles: a cylindrical rotation profile, and a shellular rotation profile. For the sake of simplicity, we have assumed the background flow to be in equilibrium with differential rotation. In the case of shellular rotation, this equilibrium would require additional forces that we have not included. In this respect, the relaxation of the incompressible assumption, or the generalization to stratified fluid bodies, will certainly be an improvement on our model.

Upon linearization of the governing fluid equations, we have revisited the propagation properties of paths of characteristics with differential rotation, in the inviscid limit. Paths of characteristics are shown to obey a second-order PDE of mixed type. Two kinds of

inertial modes are thus found to exist with differential rotation: D modes, for which the hyperbolic domain covers the entire shell, and DT modes, for which the hyperbolic domain covers part of the shell. We have analyzed the occurrence of axisymmetric ($m = 0$) and non-axisymmetric D and DT eigenmodes for various differential rotation rates and eigenfrequencies. The presence of turning surfaces for DT modes extends the range of frequencies at which inertial modes of oscillation may exist compared to solid-body rotation. We have also discussed the presence of critical latitudes and corotation resonances with differential rotation.

The analytic results based on the dynamics of characteristics are then compared to the results of numerical simulations of linear inertial waves propagating in a viscous fluid contained in a spherical shell. High-resolution calculations, based on a spectral method, have been performed to properly describe the structure of the thin shear layers arising in the physically interesting regime of small Ekman numbers (small viscosities). The Ekman numbers used in our simulations typically range from a few 10^{-9} to 10^{-6} , values that are, however, much larger than what may be expected in stars and planets (Ekman numbers between 10^{-15} and 10^{-10}). The modes that we have primarily focused on are singular modes with a shear layer converging towards a short-period wave attractor. As in the solid-body rotation case, the pattern of these shear layers is well reproduced by the dynamics of characteristics under the short-wavelength approximation. As an interesting side result, we have shown that reflexions on a turning surface, and on the body's outer radius, may form singular modes with short-period wave attractors in the whole sphere (that is, in the absence of an inner core). The damping rate of singular modes with differential rotation is also assessed in the limit of small Ekman numbers. Our results of calculations indicate that an $E^{1/3}$ scaling is to be expected for most D and DT eigenmodes, much similar to the case of solid-body rotation. Still, the case of a DT mode with damping rate approximately independent of the Ekman number is uncovered. In addition, we have carried out a qualitative analysis of the occurrence of modes with quasi-periodic orbits of characteristics for shellular rotation.

We have also briefly examined the behavior of linear inertial waves with a corotation resonance within the shell (where the wave's frequency vanishes in the frame rotating with the fluid). For cylindrical rotation, our simulations show that inertial waves may cross a corotation resonance, but experience a very large absorption at this location, much like inertial waves propagating in differentially rotating astrophysical discs (Latter & Balbus 2009). For shellular rotation, however, we have found that waves may propagate across a corotation resonance (critical layer) without visible absorption. Such modes are found to be unstable for small enough viscosities. Clearly, these findings appeal for a confirmation with an improved fluid model, where shellular rotation is balanced for by appropriate body-forces, and where non-linear effects are taken into account.

Many simplifying assumptions in the fluid model we have considered deserve further investigation to make it more applicable to the fluid flows inside stars or planets. The incompressible and homogeneous assumptions are obvious examples, and naturally a full model including appropriate modeling for the convective and radiative zones would be desirable. Since inertial waves propagate in convective regions of stars and planets, it would be interesting to study the impact of convective turbulence on the propagation and dissipation properties of inertial waves (the formation of large-scale attractors for instance). The nature and quality of wave reflections at the shell's boundaries should be analyzed, as it is still unclear for example how inertial waves reflect on the upper atmosphere of stars and planets.

We thank Henrik Latter, Richard Nelson and Gordon Ogilvie for very helpful discussions. MR would like to specially thank Susan Friedlander who suggested this work during a visit in Toulouse. Many years after, these discussions have borne fruit! We are also grateful to the three anonymous referees for their constructive reports. Numerical simulations were carried out on the CalMip machine of the Centre Interuniversitaire de Calcul de Toulouse, and on the Darwin Supercomputer of the University of Cambridge High Perfor-

mance Computing Service. CB acknowledges support from a Herchel Smith Postdoctoral Fellowship of the University of Cambridge.

Appendix A.

This appendix derives the partial differential equation satisfied by the perturbed pressure, p , in the inviscid limit. It also derives the wave dispersion relation, the phase and the group velocities under the short-wavelength approximation. In cylindrical coordinates (s, φ, z) , Eq. (2.1) becomes

$$i\tilde{\Omega}_p \mathbf{u} + 2\Omega \mathbf{e}_z \times \mathbf{u} + s(\mathbf{u} \cdot \nabla \Omega) \mathbf{e}_\varphi = \nabla p, \quad (\text{A } 1)$$

with Ω the background angular frequency and $\tilde{\Omega}_p$ the Doppler-shifted frequency. The cylindrical components of the linearized velocity vector, (u_s, u_φ, u_z) , can be expressed as a function of p and of its partial derivatives:

$$u_s(s, z) = \frac{1}{i\tilde{\Omega}_p(A_s - \tilde{\Omega}_p^2)} \times \left[\tilde{\Omega}_p^2 \frac{\partial p}{\partial s} + A_z \frac{\partial p}{\partial z} + 2\Omega \tilde{\Omega}_p \frac{mp}{s} \right], \quad (\text{A } 2)$$

$$u_\varphi(s, z) = \frac{1}{2\Omega(A_s - \tilde{\Omega}_p^2)} \times \left[A_s \frac{\partial p}{\partial s} + A_z \frac{\partial p}{\partial z} + 2\Omega \tilde{\Omega}_p \frac{mp}{s} \right], \quad (\text{A } 3)$$

$$u_z(s, z) = \frac{i}{\tilde{\Omega}_p} \frac{\partial p}{\partial z}, \quad (\text{A } 4)$$

and where

$$A_s = \frac{2\Omega}{s} \frac{\partial}{\partial s} (s^2 \Omega) \quad \text{and} \quad A_z = \frac{2\Omega}{s} \frac{\partial}{\partial z} (s^2 \Omega). \quad (\text{A } 5)$$

For solid-body rotation or cylindrical rotation, $A_z = 0$ and $A_s = 4\Omega^2$. Note the special case where $\tilde{\Omega}_p = 0$ for which a corotation resonance exists in the shell, and that where $A_s = \tilde{\Omega}_p^2$, which is analogous to Lindblad resonances in compressible fluids with cylindrical rotation such as astrophysical discs.

Taking the divergence of Eq. (A 1) and using Eqs. (A 2) to (A 4), we find, after some algebra, that p satisfies:

$$\begin{aligned} -\tilde{\Omega}_p^2 \frac{\partial^2 p}{\partial s^2} + (A_s - \tilde{\Omega}_p^2) \frac{\partial^2 p}{\partial z^2} - A_z \frac{\partial^2 p}{\partial s \partial z} = & \quad (\text{A } 6) \\ \frac{\partial p}{\partial s} \left[\frac{\tilde{\Omega}_p^2}{s} + \frac{\partial A_s}{\partial s} - \frac{mA_s \tilde{\Omega}_p}{2\Omega s} - \frac{A_s}{A_s - \tilde{\Omega}_p^2} \frac{\partial}{\partial s} (A_s - \tilde{\Omega}_p^2) \right] & \\ + \frac{\partial p}{\partial z} \left[\frac{A_z}{s} + \frac{\partial A_z}{\partial s} - \frac{mA_z \tilde{\Omega}_p}{2\Omega s} \left(1 + \frac{4\Omega^2}{\tilde{\Omega}_p^2} \right) - \frac{A_z}{A_s - \tilde{\Omega}_p^2} \frac{\partial}{\partial s} (A_s - \tilde{\Omega}_p^2) \right] & \\ + \frac{mp}{s} \left[\frac{m}{s} (A_s - \tilde{\Omega}_p^2 - 8\Omega^2) + \frac{A_s \tilde{\Omega}_p}{\Omega s} \left(1 - \frac{4\Omega^2}{A_s} \right) - \frac{2\Omega \tilde{\Omega}_p}{A_s - \tilde{\Omega}_p^2} \frac{\partial}{\partial s} (A_s - \tilde{\Omega}_p^2) \right], & \end{aligned}$$

which reduces to Eq. (3.1) when only second-order terms are retained (the short-wavelength approximation).

We now examine the propagation properties of local waves in a meridional plane. Assuming $p \propto \exp(i\{k_s s + k_z z\})$, Eq. (A 6) yields the following wave dispersion relation in

the short-wavelength approximation:

$$\tilde{\Omega}_p^2 = \frac{k_z^2}{\|\mathbf{k}\|^2} \left[A_s - \frac{k_s}{k_z} A_z \right], \quad (\text{A } 7)$$

where $\|\mathbf{k}\| = \sqrt{k_s^2 + k_z^2}$. For solid-body rotation, Eq. (A 7) reduces to the well-known dispersion relation $\tilde{\Omega}_p = \pm 2\Omega k_z / \|\mathbf{k}\|$ (see, e.g., Greenspan 1969). In the bracket term of Eq. (A 7), while $A_s > 0$ is required to satisfy Rayleigh's criterion, the sign of $A_z k_s / k_z$ is not known *a priori*. Eq. (A 7) therefore indicates that an instability may occur if $A_s - A_z k_s / k_z < 0$. It corresponds in fact to the Goldreich-Schubert-Fricke instability for an incompressible inviscid fluid (Goldreich & Schubert 1967; Fricke 1968), in which case the inequality $A_s - A_z k_s / k_z < 0$ is identical to that in equation 33 (misprinted) of Goldreich & Schubert (1967) (see also Nelson, Gressel & Umurhan (2012)). Assuming the fluid is stable against the Goldreich-Schubert-Fricke instability, we introduce

$$\tilde{\mathcal{B}} = \left[A_s - \frac{k_s}{k_z} A_z \right]^{1/2}, \quad (\text{A } 8)$$

and Eq. (A 7) translates into $\tilde{\Omega}_p = \pm \tilde{\mathcal{B}} |k_z| / \|\mathbf{k}\|$. In the frame rotating with the fluid, the phase velocity, $\mathbf{v}_p = \tilde{\Omega}_p \mathbf{k} / \|\mathbf{k}\|^2$, satisfies

$$\mathbf{v}_p = \frac{\pm \tilde{\mathcal{B}} k_z}{\|\mathbf{k}\|^3} \mathbf{k}, \quad (\text{A } 9)$$

while the group velocity, $\mathbf{v}_g = \partial \tilde{\Omega}_p / \partial \mathbf{k}$, is given by

$$\mathbf{v}_g = \pm \frac{k_s}{\|\mathbf{k}\|^3} (-k_z \mathbf{e}_s + k_s \mathbf{e}_z) \times \left[\tilde{\mathcal{B}} + \frac{A_z \|\mathbf{k}\|^2}{2 k_s k_z} \tilde{\mathcal{B}}^{-1} \right]. \quad (\text{A } 10)$$

Note that $\mathbf{k} \cdot \mathbf{v}_g = 0$: the group velocity is perpendicular to the phase velocity for differential rotation as for solid-body rotation.

REFERENCES

- BARKER, A. J. & OGILVIE, G. I. 2010 On internal wave breaking and tidal dissipation near the centre of a solar-type star. *Monthly Notices of the Royal Astronomical Society* **404**, 1849–1868.
- BRYAN, G. 1889 The waves on a rotating liquid spheroid of finite ellipticity. *Phil. Trans. R. Soc. Lond.* **180**, 187–219.
- CARTAN, E. 1922 Sur les petites oscillations d'une masse fluide. *Bull. Sci. Math.* **46**, 317–352, 356–369.
- DINTRANS, B., RIEUTORD, M. & VALDETTARO, L. 1999 Gravito-inertial waves in a rotating stratified sphere or spherical shell. *Journal of Fluid Mechanics* **398**, 271–297.
- FRICKE, K. 1968 Instabilität stationärer Rotation in Sternen. *ZAp* **68**, 317.
- FRIEDLANDER, S. 1982 Turning surface behaviour for internal waves subject to general gravitational fields. *Geophysical and Astrophysical Fluid Dynamics* **21**, 189–200.
- FRIEDLANDER, S. 1987 Hydromagnetic waves in the Earth's fluid core. *Geophysical and Astrophysical Fluid Dynamics* **39**, 315–333.
- FRIEDLANDER, S. & SIEGMANN, W. L. 1982 Internal waves in a rotating stratified fluid in an arbitrary gravitational field. *Geophysical and Astrophysical Fluid Dynamics* **19**, 267–291.
- GOLDREICH, P. & SCHUBERT, G. 1967 Differential Rotation in Stars. *The Astrophysical Journal* **150**, 571.
- GOODMAN, J. & LACKNER, C. 2009 Dynamical Tides in Rotating Planets and Stars. *ApJ* **696**, 2054–2067.
- GREENSPAN, H. P. 1969 *The theory of rotating fluids*. Cambridge University Press.
- HOLLERBACH, R. & KERSEWELL, R. 1995 Oscillatory internal shear layers in rotating and precessing flows. *J. Fluid Mech.* **298**, 327–339.
- KELLEY, D., TRIANA, S. A., ZIMMERMAN, D., TILGNER, A. & LATHROP, D. 2007 Inertial waves driven by differential rotation in a planetary geometry. *Geophysical and Astrophysical Fluid Dynamics* **101**, 469–487.
- KELLEY, D. H., TRIANA, S. A., ZIMMERMAN, D. S. & LATHROP, D. P. 2010 Selection of inertial modes in spherical Couette flow. *Phys. Rev. E* **81** (2), 026311.
- KELVIN, LORD 1880 Vibrations of a columnar vortex. *Phil. Mag.* **10**, 155–168.

- KERSWELL, R. 1995 On the internal shear layers spawned by the critical regions in oscillatory Ekman boundary layers. *J. Fluid Mech.* **298**, 311–325.
- LATTER, H. N. & BALBUS, S. A. 2009 Inertial waves near corotation in three-dimensional hydrodynamical discs. *Monthly Notices of the Royal Astronomical Society* **399**, 1058–1073.
- LE DIZÈS, S. 2004 Viscous critical-layer analysis of vortex normal modes. *Studies App. Math.* **112**, 315–332.
- MAAS, L. & LAM, F.-P. 1995 Geometric focusing of internal waves. *J. Fluid Mech.* **300**, 1–41.
- NELSON, R. P., GRESSEL, O. & UMURHAN, O. M. 2012 Linear and nonlinear evolution of the vertical shear instability in accretion discs. *ArXiv e-prints* .
- OGILVIE, G. 2009 Tidal dissipation in rotating fluid bodies: a simplified model. *MNRAS* **396**, 794–806.
- OGILVIE, G. I. 2005 Wave attractors and the asymptotic dissipation rate of tidal disturbances. *Journal of Fluid Mechanics* **543**, 19–44.
- OGILVIE, G. I. & LIN, D. N. C. 2004 Tidal Dissipation in Rotating Giant Planets. *ApJ* **610**, 477–509.
- OGILVIE, G. I. & LIN, D. N. C. 2007 Tidal Dissipation in Rotating Solar-Type Stars. *The Astrophysical Journal* **661**, 1180–1191.
- RIEUTORD, M. 1987 Linear theory of rotating fluids using spherical harmonics part I: Steady flows. *Geophysical and Astrophysical Fluid Dynamics* **39**, 163–182.
- RIEUTORD, M. 2006 The dynamics of the radiative envelope of rapidly rotating stars. i. a spherical boussinesq model. *A&A* **451**, 1025–1036.
- RIEUTORD, M., GEORGEOT, B. & VALDETTARO, L. 2001 Inertial waves in a rotating spherical shell: attractors and asymptotic spectrum. *J. Fluid Mech.* **435**, 103–144.
- RIEUTORD, M., TRIANA, S. A., ZIMMERMAN, D. S. & LATHROP, D. P. 2012 Excitation of inertial modes in an experimental spherical Couette flow. *Phys. Rev. E* **86** (2), 026304.
- RIEUTORD, M. & VALDETTARO, L. 1997 Inertial waves in a rotating spherical shell. *J. Fluid Mech.* **341**, 77–99.
- RIEUTORD, M. & VALDETTARO, L. 2010 Viscous dissipation by tidally forced inertial modes in a rotating spherical shell. *J. Fluid Mech.* **643**, 363–394.
- RIEUTORD, M., VALDETTARO, L. & GEORGEOT, B. 2002 Analysis of singular inertial modes in a spherical shell: the slender toroidal shell model. *J. Fluid Mech.* **463**, 345–360.
- STEWARTSON, K. 1971 On trapped oscillations of a rotating fluid in a thin spherical shell. *Tellus* **23**, 506–510.
- STEWARTSON, K. 1972a On trapped oscillations of a rotating fluid in a thin spherical shell II. *Tellus* **24**, 283–287.
- STEWARTSON, K. 1972b On trapped oscillations in a slightly viscous rotating fluid. *J. Fluid Mech.* **54**, 749–761.
- STEWARTSON, K. & RICKARD, J. 1969 Pathological oscillations of a rotating fluid. *J. Fluid Mech.* **35**, 759–773.
- VALDETTARO, L., RIEUTORD, M., BRACONNIER, T. & FRAYSSE, V. 2007 Convergence and round-off errors in a two-dimensional eigenvalue problem using spectral methods and arnoldi-chebyshev algorithm. *J. Comput. and Applied Math.* **205**, 382–393.
- WU, Y. 2005 Origin of Tidal Dissipation in Jupiter. II. The Value of Q. *The Astrophysical Journal* **635**, 688–710.
- ZAHN, J.-P. 1992 Circulation and turbulence in rotating stars. *A&A* **265**, 115.